Earth **Surface**
Dynamics

Alpine hillslope failure in the western US: insights from the Chaos Canyon landslide, Rocky Mountain National Park, USA

Matthew C. Morriss[1], **Benjamin Lehmann**[2,3], **Benjamin Campforts**[2,4], **George Brencher**[5], **Brianna Rick**[6,7], **Leif S. Anderson**[8], **Alexander L. Handwerger**[9,10], **Irina Overeem**[2], and **Jeffrey Moore**[8]

[1]Earth Sciences Department, University of Oregon Eugene, OR 97403, USA
[2]Institute of Arctic and Alpine Research, University of Colorado, Boulder, CO, USA
[3]Univ. Grenoble Alpes, Univ. Savoie Mont Blanc, CNRS, IRD, Univ. Gustave Eiffel,
ISTERRE 38000 Grenoble, France
[4]Department of Earth Sciences, VU University Amsterdam, Amsterdam, 1081HV, the Netherlands
[5]Civil and Environmental Engineering, University of Washington, Seattle, WA, USA
[6]Department of Geosciences, Colorado State University, Fort Collins, CO 80523, USA
[7]Alaska Climate Adaptation Science Center, Fairbanks, AK 99775, USA
[8]Department of Geology and Geophysics, Salt Lake City, UT, USA
[9]Jet Propulsion Laboratory, California Institute of Technology, Pasadena, CA 91109, USA
[10]Joint Institute for Regional Earth System Science and Engineering, University of California,
Los Angeles, Los Angeles, CA 90095, USA

Correspondence: Matthew C. Morriss (matthew.c.morriss@gmail.com) and Benjamin Lehmann
(benjamin.lehmann@univ-grenoble-alpes.fr)

Abstract. The Chaos Canyon landslide, which collapsed on the afternoon of 28 June 2022 in Rocky Mountain National Park, presents an opportunity to evaluate instabilities within alpine regions faced with a warming and dynamic climate. Video documentation of the landslide was captured by several eyewitnesses and motivated a rapid field campaign. Initial estimates put the failure area at $66\,630\,\mathrm{m}^2$, with an average elevation of 3555 m above sea level. We undertook an investigation of previous movement of this landslide, measured the volume of material involved, evaluated the potential presence of interstitial ice and snow within the failed deposit, and examined potential climatological impacts on the collapse of the slope. Satellite radar and optical measurements were used to calculate deformation of the landslide in the 5 years leading up to collapse. From 2017 to 2019, the landslide moved $\sim 5\,\mathrm{m\,yr}^{-1}$, accelerating to $17\,\mathrm{m\,yr}^{-1}$ in 2019. Movement took place through both internal deformation and basal sliding. Climate analysis reveals that the collapse took place during peak snowmelt, and 2022 followed 10 years of higher than average positive degree day sums. We also made use of slope stability modeling to test what factors controlled the stability of the area. Models indicate that even a small increase in the water table reduces the factor of safety to < 1, leading to failure. We posit that a combination of permafrost thaw from increasing average temperatures, progressive weakening of the basal shear zone from several years of movement, and an increase in pore-fluid pressure from snowmelt led to the 28 June collapse. Material volumes were estimated using structure from motion (SfM) models incorporating photographs from two field expeditions on 8 July 2022 – 10 d after the slide. Detailed mapping and SfM models indicate that $\sim 1\,258\,000 \pm 150\,000\,\mathrm{m}^3$ of material was deposited at the slide toe and $\sim 1\,340\,000 \pm 133\,000\,\mathrm{m}^3$ of material was evacuated from the source area. The Chaos Canyon landslide may be representative of future dynamic alpine topography, wherein slope failures become more common in a warming climate.

1 Introduction

The Chaos Canyon collapse took place during a sunny early-summer day at 03:31 PM LT on 28 June 2022 in Rocky Mountain National Park (RMNP), Colorado, USA (Fig. 1). The event was first reported through social media from bystanders situated at Lake Haiyaha (Fig. 1) and directly beneath the slide. These social media posts resulted in a rapid response from Earth scientists who initially sought to investigate (1) if the failure was spontaneous or part of a longer lived behavior; (2) the mechanisms contributing to this collapse – such as a landslide, the collapse of a rock glacier, and the role of cryogenic processes in general – perhaps related to climate; and (3) the amount of material mobilized by the collapse. More broadly, this investigation developed through a desire to understand whether this failure is part of the global trend toward cryosphere instability and the degradation of permafrost conditions driven by climate change (Geertsema et al., 2022; Patton et al., 2019). Mass movements in alpine regions have been documented with increasing frequency in the European Alps, Canada, and Alaska (Dai et al., 2020; Geertsema et al., 2022; Lacroix et al., 2022); however, few such observations have been made in the coterminous United States. Despite the lack of observed climate-driven landslides in the coterminous US, these high-elevation slope failures pose a potentially high risk to an ever-increasing number of people who spend time in alpine environments. RMNP was visited by ∼ 4.4 million people in 2021, making it the 14th most visited National Park in the US (NPS, 2022). As the climate warms, developing awareness around future alpine hazards within RMNP and across the broader western US cordillera is an important priority.

1.1 Stability of alpine topography

A warming climate has led to a warming of permafrost, glacier retreat, and growing instability in alpine regions across the globe (Patton et al., 2019; Shan et al., 2014). This instability is readily observed in global glacial mass inventories, with 69 % of global glacial mass loss between 1991 and 2010 being attributable to anthropogenic climate warming and only 25 % of mass loss being due to anthropogenic climate warming in the 1851–2010 period (Marzeion et al., 2014; Hugonnet et al., 2021). An increase in rockfall, landslides, and glacier retreat has been well documented in the European Alps and the alpine regions of Canada and Alaska (Cossart et al., 2008; Deline et al., 2021; Kos et al., 2016; Geertsema et al., 2022). For example, 70 % of the rockfalls to occur on the Mont Blanc massif since 1947 took place after 1991, with 83.5 % of rockfalls surveyed between 2003 and 2014 originating in areas modeled to have permafrost (Ravanel and Deline, 2011; Deline et al., 2021). Some of these destabilization events have received international news coverage (e.g., areas below the Planpincieux glacier in Italy on

the flanks of Mont Blanc) and resulted in intermittent area closures and evacuations (Dematteis et al., 2021; Giordan et al., 2020). Other events have been more remote and garnered interest from the scientific community but have not had an impact on a broader population (e.g., Lipovsky et al., 2008).

So far, few notable increases in instabilities in the alpine regions of the conterminous United States have been reported. This is despite the observations of sporadic permafrost across states such as Colorado above 3200 m above sea level (a.s.l.) and discontinuous permafrost above 3500 m a.s.l., as well as the dynamic nature of midlatitude permafrost, which may quickly thaw due to climate warming (Ives and Fahey, 1971; Slater and Lawrence, 2013; Obu et al., 2019). It remains to be seen whether mountainous terrain in the conterminous US will experience a similar increase in events like those seen in Alaska and the European Alps (O'Connor and Costa, 1993). The current geomorphological evolution of these alpine environments integrates both (1) the long-term response to glacial retreat and glacial conditioning of the topography (i.e., on scales of tens to hundreds of thousands of years) and (2) the impact of a recent changing climate (i.e., on timescales of 10–100 years) via glacier retreat and permafrost degradation (Huggel et al., 2010; Stoffel and Huggel, 2012; Obu et al., 2019). Quantifying the dynamics of mountain landforms facing climate change is proving difficult, with the effects of recent decades of warming still yet to be seen in alpine landscapes (e.g., Christian et al., 2018). Predictions of the geomorphological response such as mountain slope instability to future climate scenarios remain limited because the processes involved operate on interdependent timescales and are therefore difficult to characterize. Herein, we develop the tools necessary to analyze a high-elevation, midlatitude landslide and broaden our understanding of the stability of alpine slopes within a warming climate regime through this case study. We take a multidisciplinary approach by characterizing the relation between permafrost, topographic and climate forcings, and slope instabilities as they pertain to the 28 June 2022 failure of the Chaos Canyon landslide.

1.2 The Chaos Canyon landslide

The Chaos Canyon landslide sits above the treeline in the alpine reaches of Rocky Mountain National Park (Fig. A1). The pre-collapse landslide extended from ∼ 3450 to ∼ 3660 m in elevation. Based on pre-collapse satellite imagery, the landslide is a diamicton, composed of grains ranging from fine sediments to large boulders (∼ 10 s of m). The slide occurred along the contact between the middle Proterozoic Silver Plume Granite and the early Proterozoic biotite schists (Fig. 2) with a moderate foliation dipping to the southeast and toward Chaos Canyon (Braddock and Cole, 1990). A deposit in the bottom of Chaos Canyon was mapped by Braddock and Cole (1990) and Johnson et al. (2021) as a poten-
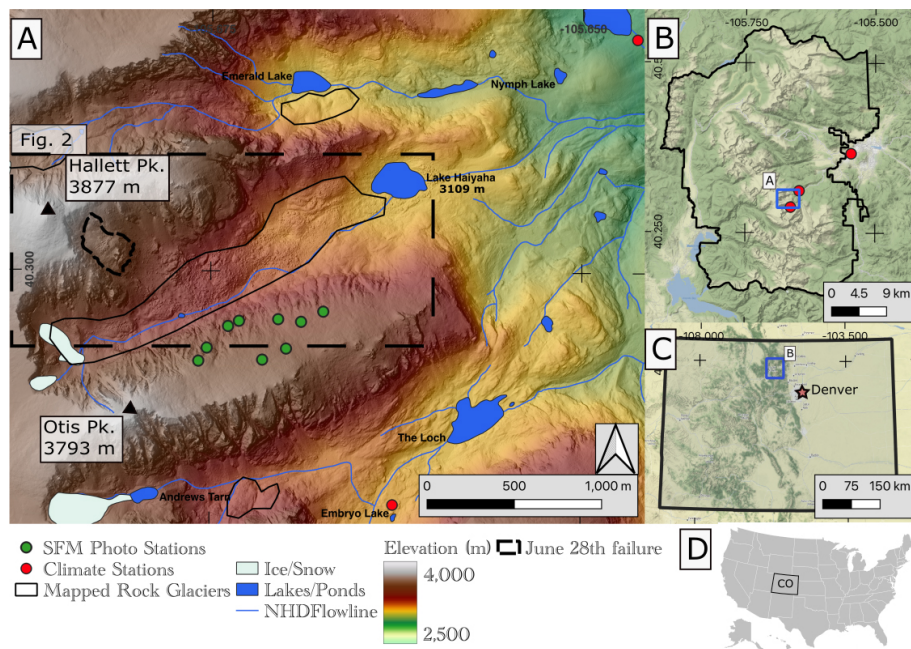
Figure 1. Overview of the landslide area. **(a)** Hillshade with hypsometric tint from a 1 m lidar digital elevation model (DEM) of the Chaos Canyon landslide and the surrounding topography. Highlighted are the outlines of mapped rock glaciers (Johnson et al., 2021), the nine photo locations used in the structure from motion survey, and the two climate stations used in climate reconstructions for the slide. Lakes, streams, and ice–snow bodies are from the National Hydrography Dataset (NHD) (USGS, 2019). Imagery predates 28 June failure. **(b)** The location of panel **(a)** within Rocky Mountain Park. **(c)** The location of panel **(b)** within Colorado, USA. **(d)** The location of Colorado **(c)** within the USA.

tially active rock glacier, with the landform that failed on 28 June mapped as Quaternary talus (Figs. 1 and 2).

1.3 Primary questions

This collapse spurred a series of questions at the scale of the landslide itself which also broaden to the scope of alpine landforms across the conterminous United States.

1. Was the landslide moving prior to its collapse on 28 June?

2. What were the climatic trends leading into the collapse?

3. Can we constrain the volume of the slide? What is this volume?

4. Can we ascertain the presence or absence of permafrost? Is there evidence of degradation of permafrost through time?

5. Can we use slope stability modeling to further evaluate the rheology of the slide and gain insights into the processes at work? For instance, can we quantify the role of groundwater?

6. What does this work tell us about the other landforms and their stability across the park and western cordillera, which is rapidly warming?

2 Methods

To answer questions posed above, we undertook a multidisciplinary investigation of the Chaos Canyon landslide and the events that led up to the failure. We combined both satellite-based image correlation using optical data and interferometric synthetic aperture radar (InSAR) to constrain movement of the landslide prior to 28 June 2022. A climatological analysis examined the role of snowmelt and whether the timing of the collapse coincided with peak snowmelt. To assess the landscape evolution impacts of the landslide, we created a structure from motion (SfM) model. We further developed climatological analysis by modeling the potential presence of permafrost or interstitial ice within the landform. Finally, we conducted a slope stability analysis to evaluate the potential factors at play in the stability of the deposit prior to collapse.

2.1 Remote sensing

To understand the processes at work leading up to and during the 28 June collapse in Chaos Canyon, it is important to investigate characteristics of landslide motion prior to collapse. As in situ survey data are unavailable, we utilized two complementary remote sensing techniques: InSAR and image correlation.
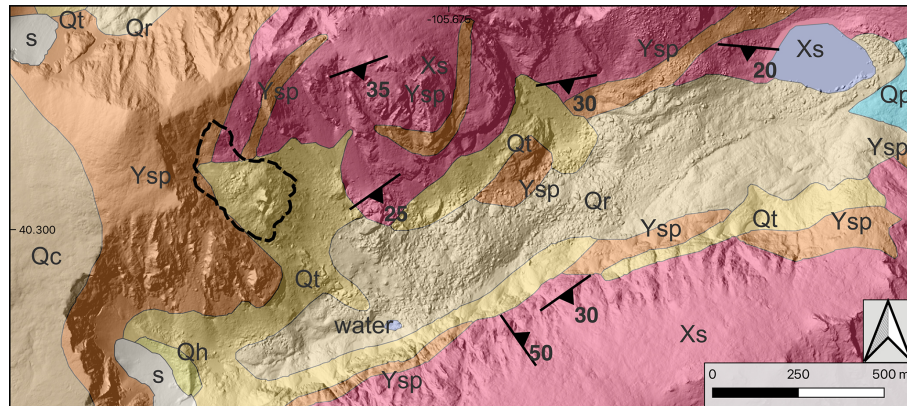
Figure 2. Geologic context of the Chaos Canyon landslide, perched above the canyon floor atop a contact between the Silver Plume Granite (Ysp) and a biotite schist (Xs). Note that there is a foliation dip toward Chaos Canyon at 35°. Other lithic designators are as follows. Qc – Quaternary colluvium; Qr – Quaternary rock glacier; Qt – Quaternary talus; Qh – Quaternary till; s – snow. Water bodies are not colored. The dashed black line is the extent of the 28 June 2022 failure. Underlying geologic data are from Braddock and Cole (1990).

2.1.1 InSAR

InSAR is a remote sensing technique that can be used to measure millimeter-scale displacement of the ground surface from space (Bürgmann et al., 2000). Interferograms are InSAR-derived maps containing information about surface displacement between two acquisition times along the satellite line of sight (LOS). To investigate rates of displacement of the landslide prior to the collapse on 28 June, we created interferograms using data acquired by the Copernicus Sentinel-1 A/B satellites. Specifically, we processed and analyzed all possible short-temporal-baseline (≤ 24 d) Sentinel-1 interferograms overlapping the study area from 15 July–15 September 2015–2021 using the Jet Propulsion Laboratory InSAR Scientific Computing Environment version 2 software (Rosen et al., 2012). Short temporal baselines were chosen to limit possible unwrapping errors during interferogram processing, which are frequently caused by features moving more than half the radar wavelength (~ 2.8 cm for Sentinel-1) between acquisitions. Stacks of 34, 35, and 42 interferograms were derived from ascending (satellite flight north and looking east) track 78, ascending track 151, and descending (satellite flying south and looking west) track 56, respectively. Interferograms were processed with six looks in range and one look in azimuth, resulting in roughly 14 by 14 m pixel spacing. A 2017 U.S. Geological Survey (USGS) 3DEP digital elevation model (DEM) with 10 m pixel spacing was used to remove the topographic component of the phase and geocode the interferograms. For each of our three interferogram stacks, we removed low-quality and noisy interferograms using a coherence threshold > 0.6. Coherence is related to the similarity of scatterers in the images that form interferograms; low coherence indicates that the target surface is changing appreciably and displacement signals are unreliable. We lastly computed the pixel-wise median where

coherence was > 0.4, yielding a single median velocity map for each track (e.g., Fig. 4).

2.1.2 Image correlation

We used image correlation to measure 2D ground displacements (east–west and north–south) at the Chaos Canyon landslide based on Google Earth and PlanetScope images. We examined all available historical Google Earth images of the site and identified two high-resolution photos that had little snow coverage and no visible artifacts. The images selected were from September 2016 and August 2019. Before exporting the images, we turned off terrain and 3D effects, as well as image compression and filtering. We selected the maximum available image output resolution of 8192×4925 pixels from Google Earth Pro. Scaling of the images from pixels to meters had to be manually evaluated; for this we measured several distances on each image in Google Earth and then determined the corresponding pixel dimensions, resulting in a scaling value of 0.21 m per pixel. We then applied an image correlation approach based on fast Fourier transform that first aligns the image pair with a co-registration routine, then evaluates internal misalignments using a moving window to measure displacements in the plane of image (Bickel et al., 2018). We used a window size of 256×256 pixels with 50 % overlap, resulting in ~ 27 m resolution outputs, and a vector-based post-processing filter (for details see Bickel et al., 2018).

In addition, we calculated the time-dependent displacement of the landslide between 2017 and 2021 using PlanetScope imagery (3 m pixel resolution). We selected five images acquired during the snow-free period (either from August or September each year). Unfortunately, there were no snow-free images in 2022 prior to the failure of the slope. The PlanetScope images are orthorectified and have radiometric, geometric, and sensor corrections applied (Planet-

Team, 2017). We performed image correlation on 10 image pairs with a minimum time span of ~ 1 year and a maximum time span of ~ 4 years between images (Table A1). For image correlation analysis using PlanetScope imagery, we used the outlier-resistant correlator (OR-Corr) subpixel image correlation method (Milliner and Donnellan, 2020). We used a 33×33 pixel correlation window with a step size of nine pixels, resulting in 27 m pixel resolution displacement maps. We then used the MintPy time series software (Yunjun et al., 2019) to invert for the time-dependent motion of the landslide.

2.2 Climate analysis

To better understand the climatic circumstances of the 28 June collapse, we analyzed the records at the Bear Lake SNOwpack TELemetry Network (SNOTEL), from the United States Department of Agriculture and Natural Resources Conservation Service, 2022) located ~ 3 km to the northeast of the landslide. Specifically, we wanted to test the hypothesis that snowmelt may have contributed to the catastrophic failure. We extracted the Bear Lake Climate SNOTEL (Fig. 1) temperature record going back to 1991 (NRCS, 2023). This meteorological site is located at 2903 m a.s.l. We made use of the Global Historical Climatology Network site (USR0000CEST) located in Estes Park at 2382 m a.s.l. (Fig. 1) to determine a local environmental lapse rate of 4.65×10^{-3} °C m^{-1}. This lapse rate was calculated by examining the average daily temperature difference between these two sites and dividing by their difference in elevation. We then shifted the temperature record collected at Bear Lake to reflect the environment at the top of the slide at ~ 3147 m a.s.l. We made a cumulative positive degree day sum (PDDS) of the temperature record representative of conditions at the top of the slide (Braithwaite and Hughes, 2022). PDDS is a cumulative sum of the average daily temperatures greater than 0 °C. By applying a global average snow ablation rate of ~ 4.5 mm d^{-1} °C^{-1} (Anderson et al., 2014), we estimated spring snowmelt atop the Chaos Canyon landslide.

2.3 Structure from motion

A DEM of the 28 June collapse was obtained using SfM and terrestrial photogrammetry. Data collection took place on 8 July 2022, 10 d after the collapse. Photographs were taken from nine different stations to the east of Otis Peak Ridge, providing a direct view of the landslide (Fig. 1 and Table A2). Photo acquisition was made between 10:30 and 15:00 LT, ensuring ideal light conditions. We used a Sony Alpha a7S III Mirrorless Digital Model with a Tamron 28–200 mm f/2.8-5.6 Di III RXD lens mounted on a tripod. The following settings were used for all pictures: a focal length of 8.0, iso 400, zoom of 70 mm, and shutter time between 1/800 and 1/1250 s. Pictures were taken with approximately 80 % of overlap between them. The coordinate of each sta-

tion was recorded using a handheld GPS (Garmin GPSmap 64s). This post-collapse DEM was compared to a reference DEM (before the event) to (i) record the new geometry of the area and (ii) quantify the amount of erosion and deposition involved. The reference 1 m DEM is provided by the USGS program National Map 3DEP and was acquired in 2017.

The 3D point cloud was created with Agisoft Metashape Professional using 305 photographs. The photographs were first aligned with high accuracy, setting the key point limit to 4000 and the tie point limit to 100 000. The resulting sparse point cloud was filtered using a reconstruction uncertainty criterion of 300. The camera locations were estimated with a total error of 40 m (X error of 22.1 m, Y error of 10.3 m, and Z error of 31.7 m). We used the reference 1 m DEM from USGS to create virtual ground control points (GCPs; Fig. 3). Those GCPs were chosen outside and around the landform affected by the destabilization on bedrock features that are recognizable in both the reference DEM and the photographs acquired after the event. This approach produced five GCPs with total location error of about 0.7 m (X error of 0.04 m, Y error of 0.09 cm, and Z error of 0.13 cm; see Table A3). Finally, we produced a dense cloud made of 20×10^6 points that we converted into a DEM of 0.26 m per pixel resolution with a point density of 14 points m^{-2}. Irregularities in the obtained DEM were further removed using the following sequence of steps. First, an iterative procedure was used to identify all local depressions in the DEM (Barnes et al., 2014). These were subsequently filled using an inverse distance weighing algorithm. This step was repeated until all local minima were removed. In a second step, positive spikes in the DEM were identified using a slope-based DEM filter. These spikes were subsequently removed and resulting gaps were interpolated using the iterative procedure described above. Then the smoothed post-collapse DEM was subtracted from the pre-collapse DEM (2017) to construct a DEM of difference (DoD), from which volumes of erosion and deposition can be calculated. We also calculated simple empirical length and height metrics to compare this landslide to other landslide inventories.

2.4 Permafrost modeling

To explore the soil and bedrock temperature profile at the time of the 28 June collapse, we used a coupled model of snow and permafrost, consisting of an empirical snow model (ECsimplesnow) and the Geophysical Institute Permafrost Laboratory (GIPL) (Brown et al., 2003; Jafarov et al., 2012; Overeem et al., 2018). GIPL is a one-dimensional heat flow model, simulating ground temperature evolution and the depth of the active layer by solving nonlinear heat equations with phase change. GIPL is often set up as a spatial grid consisting of adjacent columns; however, we have little information on the soil and debris cover thickness or spatial variability in snow depth. Therefore, we chose to model the
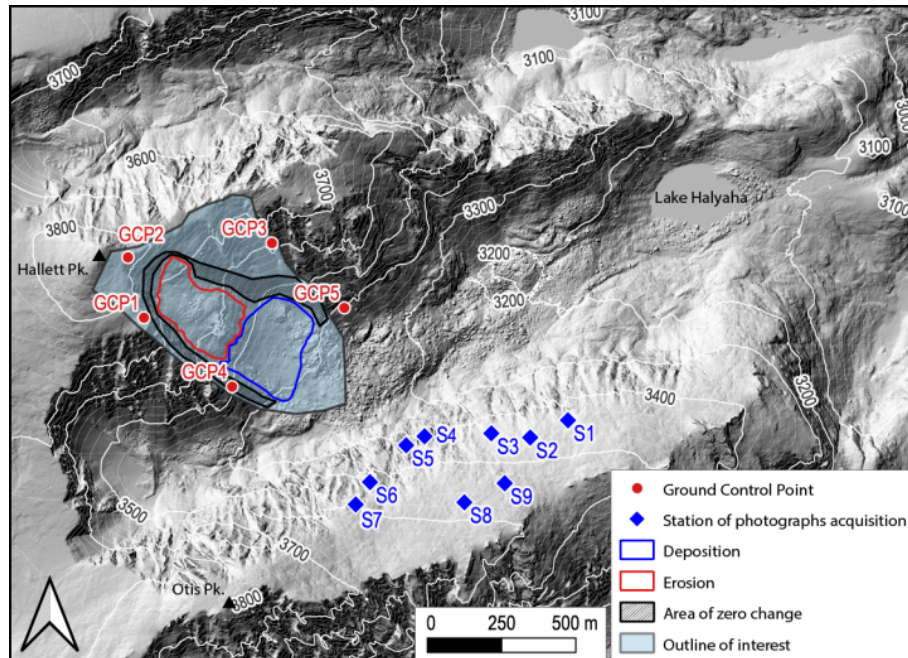
Figure 3. Location of the stations where the photographs where acquired (S) and the ground control points (GCPs) used to create the post-collapse DEM. Hillshade and elevation lines were computed using the 1 m DEM provided by the USGS program National Map 3DEP and acquired in 2017. Areas of erosion and deposition were derived from differencing the 2017 DEM and our 8 July SfM DEM.

annual evolution of subsurface temperature for a single vertical column.

We initialized subsurface properties needed for the GIPL model with soil characteristics from global soil data released in SoilGrid (Hengl et al., 2014). Key properties include soil texture and water content. We had no in situ data, but the pre-collapse satellite imagery indicated an existing diamicton – consisting of sediment and boulders. For our simulations, we assumed ~ 30 cm regolith soil, 2.7 m debris with coarse unweathered sediment, and bedrock beyond that depth. Coarse-grained sediment and bedrock then define the frozen and unfrozen thermal conductivity and heat capacity according to relationships established from laboratory experiments (Goodrich, 1982; Kersten, 1949; Schaefer and Jafarov, 2016).

We ran the combined model over the 2021 water year (1 October 2020 to 30 September 2021), with a time series of daily air temperature and precipitation, as extrapolated from observations at the Bear Lake station (as described in Sect. 2.2). Soil or bedrock temperatures were strongly modulated by snow cover over winter due to its low thermal conductivity (Zhang, 2005). The effect is complex, and ground temperature can either be lower or higher than the snow surface or air temperature, depending upon the timing, duration, and thickness of the seasonal snow cover and the air temperature history. The spatially variable but locally large wind-drifted snow accumulations in cirques in the Rocky Mountains act as a thermal insulator on an annual basis. Our re-

gional snow model, from the original empirical parameterization of Brown et al. (2003), used daily precipitation input over the water year and combined this with a snow classification map (Sturm et al., 1995) to establish snow thickness and density. This is numerically implemented in the ECsimplesnow model and coupled with the GIPL model. The landslide sits between ~ 3450 and ~ 3660 m a.s.l., which is well above the regional treeline, so vegetation coverage was set to be "open terrain", meaning that trees or extensive shrubs do not impact the snow properties.

2.5 Slope stability modeling

To explore the conditions that led to collapse of the deposit, we used the limit equilibrium analysis (e.g., Duncan, 1996) program Slide2 (Rocscience, 2021). For the analyses, we imported pre-collapse topography based on the lidar DEM of Rocky Mountain National Park. To estimate the boundary between the pre-collapse deposit and the underlying bedrock we extrapolated a surface under the pre-collapse deposit based on known bedrock outcrops on either side of the post-collapse deposit in QGIS. The underlying bedrock topography was estimated by adjusting contours, converting the contours to point data, and then re-rasterizing the data using the *GDAL_rasterize* command in QGIS.

Slide2 was used for the limit equilibrium analysis. Because the collapse occurred during the snowmelt season, we explored the stability of the pre-collapse deposit to changes in water table depth. We chose to focus on this parame-

ter related to slope stability because so little information was available regarding the landslide before its 28 June collapse. Most of the information we do have is on the rate of snowmelt and presence of permafrost. Material properties of the landslide were tuned based on our knowledge of the site from in situ observations, pre-collapse velocity data, and permafrost modeling. We modulated the landslide and underlying bedrock densities (2000 kg m^{-3} for the deposit and 2700 kg m^{-3} for the bedrock). We added a shear plane between the deposit and bedrock. We then tuned the properties of the shear plane and deposit to represent a global minimum factor of safety slightly greater than 1 (actual FoS of 1.037) to represent the observed condition that the landslide was moving prior to collapse (see Sect. 3.1.2); we hypothesized that this indicates a well-developed shear plane (Fig. 11). For the shear plane, we assume a cohesion of 1 kPa and a friction angle of 30°, while for the ice-cemented deposit we assume cohesion of 250 kPa and a friction angle of 50°.

In this model, we assume a Mohr–Coulomb failure criteria for the pre-collapse deposit and underlying bedrock (Labuz and Zang, 2012). We compared the pre-collapse global minimum factor of safety in cases with and without a slight rise in local water table. The factor of safety is the ratio of resisting forces and driving forces (e.g., Duncan, 2000). When the factor of safety is greater than 1 the slide is stable; when the factor of safety is less than 1 the slide will fail. The specific details of the model domain are described below.

3 Results

3.1 Pre-collapse movement

3.1.1 InSAR

For all tracks, median coherence within the landslide boundaries was low (0.36 ± 0.17 for ascending track 78, 0.37 ± 0.16 for ascending track 151, and 0.52 ± 0.16 for descending track 56; Fig. 4d). A total of 12 wrapped interferograms from ascending tracks 78 and 151 show clear evidence of landslide displacement beginning in August 2015 (Figs. 4b and A2a, A3). Median LOS velocities in the landslide were not distributed in a manner consistent with cohesive downslope displacement. Instead, we observed patches of apparent upslope and downslope LOS velocity, along with patches of apparently stable area, scattered across the landslide surface in no clear pattern, which is due to unwrapping errors caused by the high deformation gradient (Figs. 4b, A2a, and 6; Itoh, 1982; Handwerger et al., 2015). Thus, the median velocity does not provide a reliable indicator of landslide activity. By comparison, for all tracks, a rock glacier in the cirque to the north has a more spatially consistent downslope velocity signal (Fig. 4b), while rocky, flat areas above and below the landslide appear mostly stable outside of topography-correlated atmospheric noise.
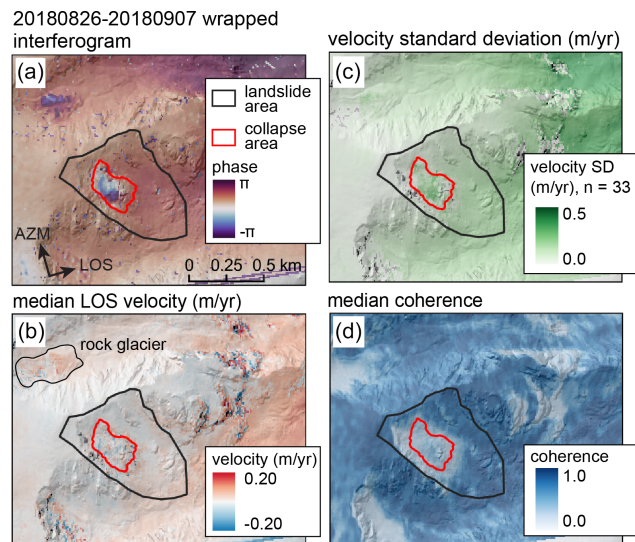

Figure 4. InSAR-derived LOS velocity of the landslide prior to the 28 June collapse. Interferograms come from Sentinel-1 ascending track 151. **(a)** A wrapped interferogram from the summer of 2018 showing clear landslide deformation of roughly 10 cm in 12 d. **(b)** Median LOS velocity of the failure area and landslide area. Interferograms with short temporal baselines and high median coherence on the landslide slope were used to create the velocity map. Positive values (red) correspond to motion away from the satellite along the satellite LOS. Note the spatial inconsistency of signals within the landslide. Negative velocity values at lower elevations are caused by topography-correlated atmospheric noise. **(c)** Standard deviation of LOS velocity. **(d)** Median coherence of the failure area and landslide area.

3.1.2 Image correlation

Google Earth

Results of digital image correlation (DIC) analysis are shown in Fig. 5. We observe a broad area of relatively large-magnitude displacement corresponding to the top surface of the landslide: in the ~ 3 years (i.e., the period 2016–2019) between images this area moved on average 10.5 ± 0.5 m (Fig. 5b). Maximum displacements of 11.5 m were found on the northern portion of the slide surface. The main landslide body showed southeast-trending movement with consistent displacement vectors (Fig. 5c). Areas of low correlation between images, and those which were filtered in post-processing, were located in the region covered by snow in the 2019 image (Fig. 5a) and near the toe of the slope (Fig. 5b). We also observed an adjacent movement near the northern head of the landslide with lower-magnitude displacements (~ 2 m) and more southerly oriented movement than the main body. Here it appears that a portion of the talus adjoining the main slide body is moving in response to motion of the main slide away from its toe. A visible scarp had developed in the 2019 image at the head of this smaller sliding body. The mean displacement azimuth for the main slide
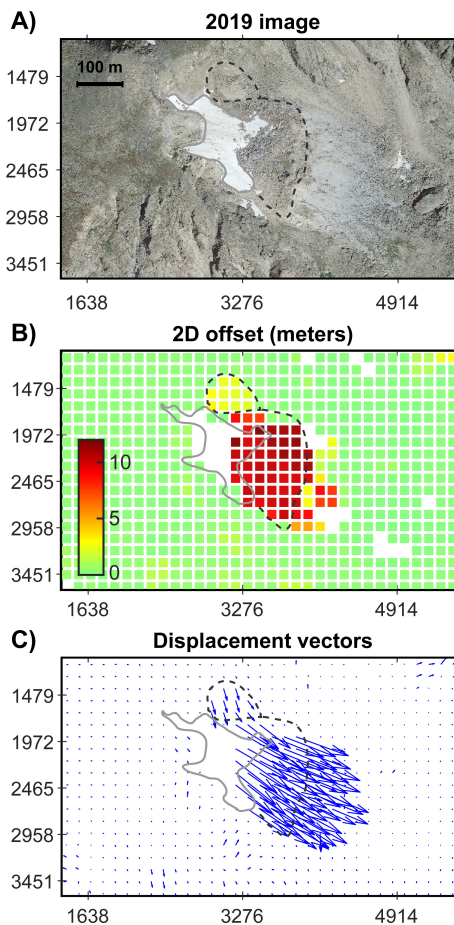
Figure 5. Results of digital image correlation for the Chaos Canyon landslide comparing © Google Earth imagery from September 2016 and August 2019. **(a)** A 2019 photo of the slide with a snow patch highlighted (solid gray line). Dashed lines highlight the crest of the main slide as well as a smaller adjoining slide thought to be secondary in response to undermining. **(b)** Scaled 2D offset magnitude. Blank cells are areas omitted during filtering; these mostly occur in snow-covered areas and at the toe of the steep frontal slope. Movement of the main body is 10.5 m on average. **(c)** Displacement vectors. The main Chaos Canyon slide and secondary adjoining slide show different displacement magnitude and orientation (dashed lines repeated from **a**). Coordinates are pixels in east (x) and north (y) orientations; image scaling is approximately 0.21 m per pixel.

body is 117° clockwise from north, while the smaller northern portion is moving at an azimuth of 162°. Finally, movement detected on and at the toe of the steep frontal slope has similar orientations only slightly lower in magnitude than at the crest (~ 8 m). This may indicate evidence supporting a basal sliding mechanism for slide movement that together with some amount of internal shear could generate the displacement pattern measured (Fig. 5b).

We can assess uncertainty in our image correlation results by measuring estimated movements in stable areas not an-

ticipated to experience movement in the period between image acquisitions. For this, we evaluate a portion of the results on the broad south slopes of Hallet Peak and find that resolved mean movements are 0.3 ± 0.1 m, well below the measured displacement of the landslide. While the image comparison shows significant displacement of the landslide between 2016 and 2019, no information is available from this analysis on when this movement might have occurred during the interval. Finally, while the relative displacements are robust, our use of Google Earth imagery requires empirical scaling assessment done on a case-by-case basis and not benefiting from the pixel dimension information or metadata from the original acquisition. This leads to some uncertainty in the absolute scaling of the displacement magnitudes. However, scaling measurements across the images, together with independent measurements of displaced boulders visually identified in the images, are consistent with displacement magnitude inferred from image analysis.

PlanetScope

Image correlation of the PlanetScope imagery is in general agreement with the spatial extent and magnitude of the actively deforming slope measured with the Google Earth imagery. Our time series analysis reveals that the landslide moved as a coherent unit but exhibited different rates spatially. The median cumulative displacement of the landslide was $\sim 29 \pm 3.5$ m ($\pm$ standard deviation) between 2017 and 2021. The maximum cumulative displacement was ~ 39 m and the minimum was ~ 20 m. The velocity increased monotonically between 2017 and 2021 but exhibited a distinct acceleration point starting in the summer of 2019. The median velocity across the landslide was $< 5\,\mathrm{m\,yr^{-1}}$ prior to 2019 and then increased to $\sim 17\,\mathrm{m\,yr^{-1}}$ by 2021. This change in kinematics starting in the summer of 2019 suggests a change in stability conditions of the slope. We also assessed the uncertainty by examining the apparent movement in a stable area. We found that the stable slope exhibited apparent displacements $< 1.3 \pm 0.27$ m. We also explored the inverse velocity relationship often used to predict landslide failure (e.g., Fukozono, 1990; Voight, 1989) but found that it yielded poor results. We did not pursue this line of inquiry further. For a direct comparison between our methods based on Google Earth and Planet imagery, please see Fig. A5.

3.2   Snowmelt rates

Our detailed climate analysis shows that the Chaos Canyon landslide collapsed as average daily temperatures were increasing to their summer peak ~ 21 d later (Fig. 7a). The year 2022 was not atypical compared to previous years over the last 3 decades. It was not remarkably warmer than past years in the winter months, nor were spring temperatures significantly warmer than typical. However, the temperature series does indicate that the collapse may have taken place
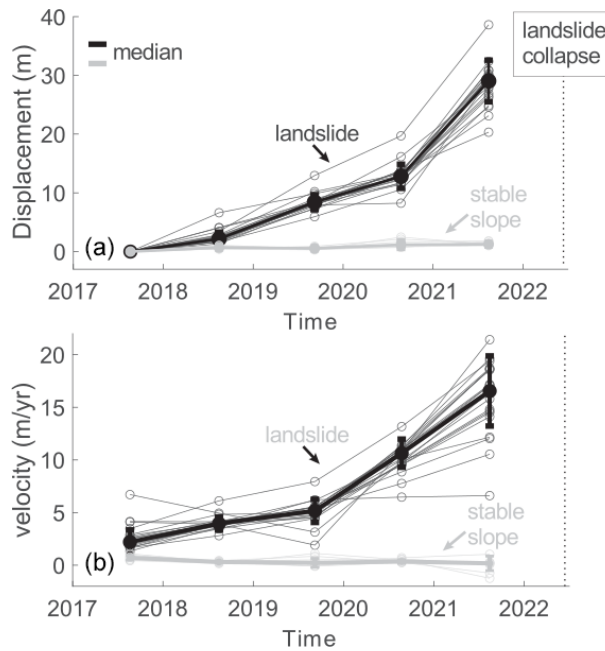
Figure 6. Image correlation results from Planet images taken in 2017, 2018, 2019, 2020, and 2021. **(a)** The thin gray lines are horizontal displacements of every pixel mapped within the landslide. The black line is the mean displacement with 1σ bars. The thick gray line shows the same statistic but for stable areas outside the landslide. A greater sampling of Planet images reveals increasing displacements moving toward the present. **(b)** The mean and 1σ uncertainty envelopes of velocity and for the landslide (black) and pixels examined outside of the footprint of the landslide (gray). The pixels outside the landslide show no systematic movement compared with the accelerating landslide.

as warming increased the rate of snowmelt. This observation is further supported by the cumulative snowmelt we calculated at the elevation equivalent with the top of the landslide (Fig. 7b). Snowmelt begins in April with melt increasing rapidly after 1 June. Compared with the 1990–2021 seasons, 2022 had slightly higher melt than most of the previous 32 years, with the 11th highest calculated melt from April–1 July. Notably, 2018, 2020, and 2021 had greater snowmelt than the 2022 season, making 2022 unremarkable in terms of snowmelt volumes. However, these calculations do indicate that the collapse took place during the peak snowmelt for the spring season (Fig. 7b). This is bolstered by the Planet imagery in Fig. 8. Panel (a), 2 June through 24 June, shows a significant decrease in snow extent across the landslide in clear accordance with the snowmelt calculations in Fig. 7b.

3.3 Change detection

The obtained difference map delineating areas of deposition and erosion associated with the collapse is highlighted in Fig. 9. Delineation of these zones was done based on regions of zero surface change (green areas) before and after event el-

evation data. Towards the edges of Fig. 9 some artifacts start to appear in the data, which can be attributed to lower point densities used during the SfM procedure in the boundary areas.

Uncertainty of the post-collapse DEM is obtained by calculating the root mean square error (RMSE) between the reference lidar DEM and the post-event DEM for a region surrounding the erosion and deposition features that were minimally disturbed (visually determined in the field). The RMSE equals 2.39 m for this region, a value that is used to estimate uncertainty ranges for total erosion and deposition volumes. The erosion area covers $55\,639\,\mathrm{m}^2$ and experienced average erosion of $24.09 \pm 2.39\,\mathrm{m}$ or a corresponding volume of $1\,340\,000 \pm 133\,000\,\mathrm{m}^3$. The deposition area covers $64\,477\,\mathrm{m}^2$ and experienced average deposition of $19.52 \pm 2.39\,\mathrm{m}$ or a corresponding volume of $1\,258\,000 \pm 154\,000\,\mathrm{m}^3$. Erosion and deposition volumes are similar within uncertainty ranges. The deposited volume is slightly lower than the eroded volume, which could be due to errors during the SfM DEM production or because of sediment evacuation towards downstream areas during and following the event.

3.4 Permafrost modeling

The steep front of the pre-failure landslide averages a slope of $\sim 40°$, greater than a typical angle of repose, which could be indicative of interstitial ice holding the deposit together (Carson, 1977; Whalley and Martin, 1992). Further investigation of the potential for interstitial ice through ground temperature modeling indicates that permafrost conditions persist to at least 15 m depth in the pre-collapse deposit (Fig. 10). For the 2020–2021 model year minimum simulated surface temperature was $-4\,°C$, maximum simulated surface temperature was $16\,°C$, and the mean surface temperature was $2\,°C$. For transient simulations through the 2020–2021 water year the thaw front propagated to 0.96 m depth by 28 June, the date of failure. These results are only relevant for the portions of the pre-collapse deposit that were snow-free. The deepest the simulated thaw front reaches, i.e., the maximum active layer depth, is $\sim 1.85\,\mathrm{m}$ at the end of the hydrological year in October (Figs. 10 and A4). Importantly, these results do confirm the presence of continuous permafrost across the landslide but do support the presence of permafrost. Data on snow insulation toward the top of the slide, which would reduce the likelihood of permafrost stability, are not available.

3.5 Slope stability modeling

To explore the role of snowmelt as a potential trigger of the landslide, we simulated a slight rise in the water table within the pre-collapse deposit. We expect that a basal shear plane is well developed at the base of the pre-collapse deposit because the landslide has been accelerating and has undergone large displacements (Figs. 5 and 6). The inclusion of this wa-
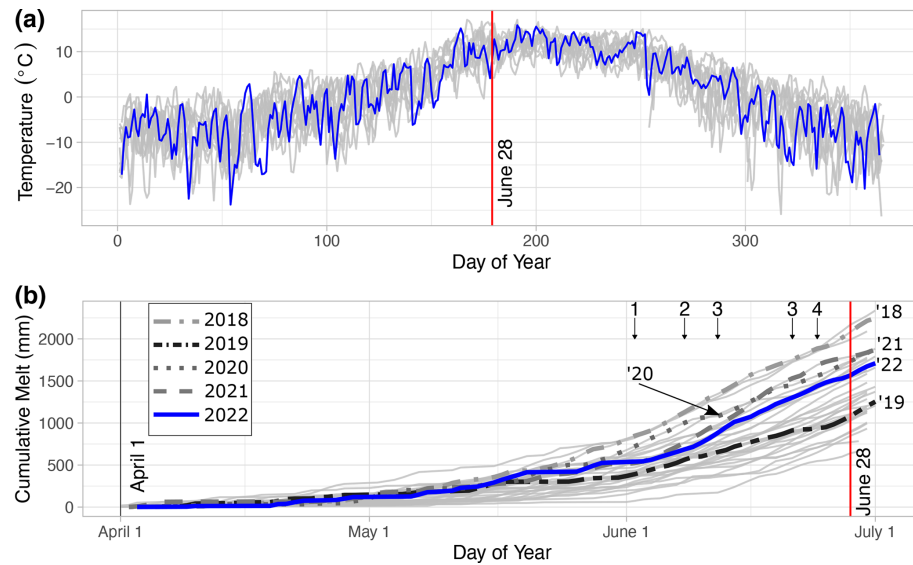
Figure 7. Climate analysis of the Chaos Canyon landslide. **(a)** The mean daily temperature series estimated for $\sim 3668\,\text{m}$, the elevation at the top of the slide. The year 2022 is highlighted in blue. Temperature series for 1990 through 2021 are gray lines. The collapse occurred on 28 June 2022. **(b)** The calculated cumulative snowmelt for the past 32 springs. The year 2022 is the blue line, with 1990–2021 snowmelt seasons shown in gray. Inset numbers highlight dates for frames from Planet imagery in Fig. 8. The snowmelt curves for the previous 4 years (2018, 2019, 2020, and 2021) are also highlighted.

ter table reduced the resistive forces in the system, leading to a global minimum factor of safety of 0.995 and thus failure of the landslide. The pre-collapse deposit thus appears to be highly sensitive to a reduction of normal stress associated with a rising water table, likely associated with spring snowmelt.

4   Discussion

Rapid environmental change is predicted to increase the occurrence of landslides and rock failures in high, alpine terrain (Ravanel and Deline, 2011; Patton et al., 2019; Deline et al., 2021). Nevertheless, few alpine rock failures linked to climate change have been documented in the conterminous United States. The Chaos Canyon landslide affords insights on the role of mass wasting in alpine terrain through abundant field and remotely sensed data as well as numerical scenario modeling. In the following, we discuss changes leading up to the event that could serve as tools to monitor future landscape stability.

4.1   Pre-collapse movement and potential causes of the 28 June collapse

The 28 June collapse of the Chaos Canyon landslide appears to have been an event lacking a well-documented modern analog in alpine regions of the conterminous United States. Image correlation results provide evidence of accelerating pre-collapse displacement at least as early as summer 2017, suggesting that unstable conditions developed over the

course of years as opposed to within a single spring snowmelt season (Figs. 5 and 6). It is important to note that inconsistencies in InSAR-derived median LOS velocities over the surface of the landslide suggest that our short-baseline interferograms suffered from unwrapping errors. This interpretation is consistent with median LOS velocities of more than $0.93\,\text{cm}\,\text{d}^{-1}$ during 15 July–15 September 2015–2021. Henceforth, we only discuss displacement rates derived from our image correlation efforts.

Initial rates of horizontal displacement were slow at $\sim 5\,\text{m}\,\text{yr}^{-1}$ between 2017 and 2019, but the landslide rapidly accelerated after 2019 to a moderate rate of $\sim 17\,\text{m}\,\text{yr}^{-1}$ (for velocity classes see Cruden and Varnes, 1996). We identified no clear climatological forcing that led to the acceleration in 2019; however, there is the potential for a progressive weakening of the failure surface beneath the landslide (Eberhardt et al., 2016) and/or potential slip localization to a single shear plane with landslide movement (Viesca and Rice, 2012; Scuderi et al., 2017). Both of these phenomena suggest that through continued and repeated movement of the landslide, the landslide weakens and accelerates until its ultimate catastrophic failure. Similar behavior, wherein increases in sliding velocity result in weakening of the failure surface, has been modeled to occur in fault zones (Ito and Ikari, 2015). Given that the Chaos Canyon landslide has several years of slow and then accelerating movement, it is a strong candidate for further analysis of potential rate weakening or shear zone development.

We can infer the potential impacts of a warming climate on this alpine landslide from the long-term trend in temperature.

A Pre-slide

June 2, 2022

June 12, 2022

June 21, 2022

June 24, 2022

B Post-slide

Landslide outline
Erosional area
Landslide deposit

0   500 m

July 1, 2022
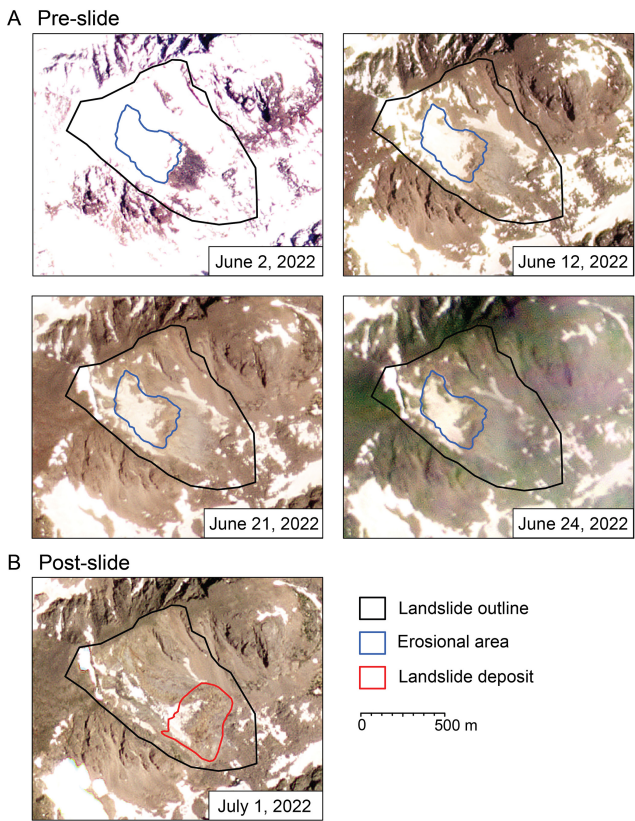
Figure 8. Planet imagery of upper Chaos Canyon in the days preceding the collapse (**a**: pre-collapse). Images are from 2, 12, 21, and 24 June. Frames show a decrease in snow coverage. Frames are also referenced in Fig. 7b. Satellite imagery further supports the conclusion that the landslide collapse took place during a period of rapid snowmelt (**b**: post-collapse). The landslide deposit after the 28 June collapse is highlighted. Pieces of the permanent snow patch have been translated with the landslide. Imagery thanks to Planet-Team (2017).

Temperature trends at the top of the landslide, approximated from the Bear Lake SNOTEL, show a clear warming signal across the past 3 decades (Fig. 12a and b), with a consistent positive temperature anomaly after 2009. Warming temperatures have been documented to correspond to landslides in both high-elevation and high-latitude landscapes, particularly where permafrost or ground ice is present (e.g., Cossart et al., 2008; Deline et al., 2021; Patton et al., 2019). Increased temperatures lead to permafrost thaw and decrease slope stability through either a change in the physical conditions of the slope (e.g., reduced cohesion) or hydrologic conditions (e.g., increased pore pressure and hydrologic conductivity; Patton et al., 2019).

The presence of permafrost conditions (Fig. 10) in the pre-collapse deposit opens the possibility that ice occupied interstitial spaces between clasts (Kenner et al., 2017; Eriksen et al., 2018). If a continuous ice layer was present within the pre-collapse deposit, snowmelt may have been channeled to

locations where tension cracks were present through the pre-collapse deposit (e.g., Mutter and Phillips, 2012). If abundant interstitial ice was present, then the entire pre-collapse body may have been moving downslope due to internal deformation and sliding. Satellite imagery of the steep front of the pre-slide deposit suggests that ice was exposed there in gullies; additionally, the pre-slide front was steeper than the angle of repose, indicating the presence of internal ice (Carson, 1977; Whalley and Martin, 1992). However, the lack of observed ice in the post-failure deposit suggests that interstitial ice may not have been abundant, though internal heating during the slide could have also melted any internal ice (Pudasaini and Krautblatter, 2014). Further model simulations should explore the interaction between percolating meltwater and permafrost within the pre-slide deposit to determine the potential for the presence of interstitial ice through the pre-slide body.

We hypothesize that permafrost within the slide deposit thawed and became intermittent due to the changing climatic conditions within Chaos Canyon over the last ∼ 30 years, likely reducing the stability of the landform. Coincident with warming temperatures, we observed an increasing rate of horizontal displacement of the landslide over the past 5 years, with evidence suggesting both basal sliding and internal deformation (Figs. 5 and 6). Thawing permafrost, combined with internal deformation and some surface cracking (Fig. 5), may have provided an increased availability of flow paths for snowmelt and rain to penetrate into the slide mass, increasing the hydrostatic pressure and promoting destabilization of the deposit on 28 June (Figs. 7b, 11, and 12c; Bogaard and Greco, 2016). Building on this discussion, we further posit that the 28 June collapse is likely due to a combination of factors: continued rate weakening and localization of a shear plain beneath the landslide in concert with a decrease in permafrost throughout the landslide. The former primed the landslide to be more sensitive to pore-water pressure increases, even from an unexceptional snowmelt year like 2022, and the latter provided more pathways for snowmelt to ultimately reach the failure plane and increase the pore-fluid pressures to the point of failure. Additionally, the adverse dip of the underlying Proterozoic biotite schists may have played a role in mobilizing some of the landslide downslope (Fig. 2).

4.2　Landslide characterization

To better understand the processes at work in the Chaos Canyon landslide and to compare this landslide to other landslides, we used a few common empirical metrics that also inform landslide rheology and processes. Landslide mobility is commonly expressed using the ratio between the maximum length of the sediment travel path (L) and the difference between the highest and lowest point impacted by the landslide (H) (Geertsema et al., 2009). The L/H ratio is a useful metric in hazard assessment because it indicates how far downstream landslide-derived material can reach from
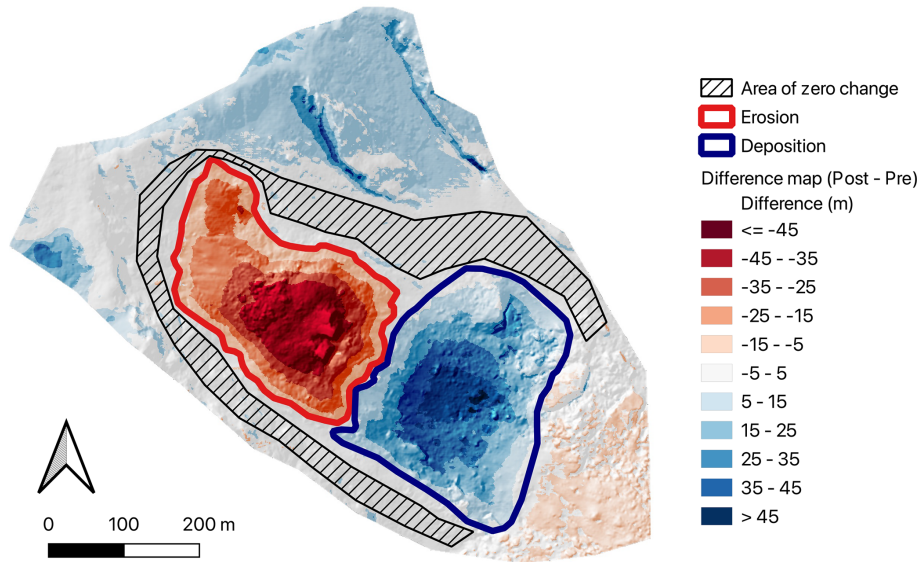
Figure 9. DEM of the difference between post- and pre-event topography. Negative values indicate erosion (red), positive values indicate deposition (blue), and green values indicate regions of zero change. The dashed area indicates regions where no visible change took place during the event and were used to calculate the accuracy of the DEM.
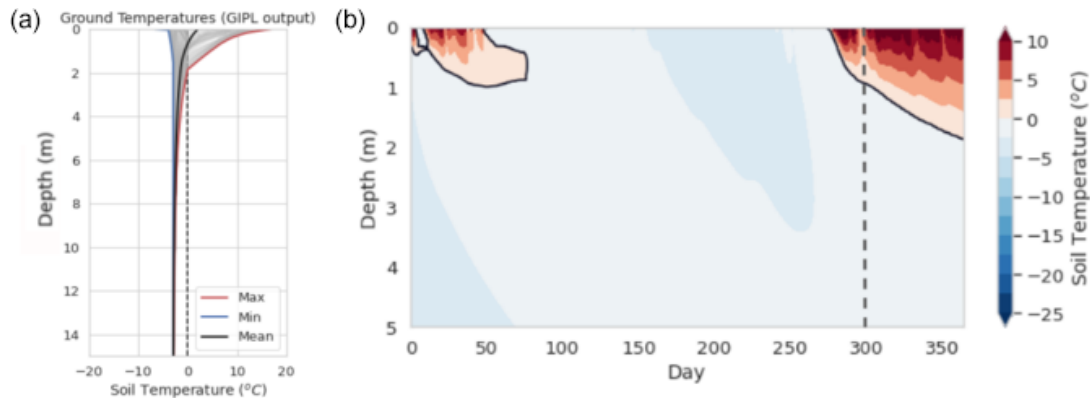

Figure 10. Simulation results of the combined snow and soil temperature model over the water year from October 2020–October 2021. Panel **(a)** shows soil temperature as a function of depth, with even maximum temperatures below $\sim 2\,\mathrm{m}$ depth never reaching above $0\,°\mathrm{C}$. Panel **(b)** shows soil temperatures with depth at the Chaos Canyon landslide across a single water year. This result mirrors the depth of the active layer shown in **(a)**. The dashed vertical line is 28 June. Note that the days are based on zero as 1 October, the start of the water year.

any given source area (Iverson et al., 2015). Several studies have also shown a positive relation between the volume of mobilized material (V) and the mobility index (L/H). A compilation of this mobility index versus landslide volumes is given in Fig. 13a. The Chaos landslide has a mobility value of $L/H \approx 1.8$ and fits within ranges of earlier documented rockslides of similar volumes (Fig. 13a). The total inundated area of the Chaos landslide (m^2) also follows earlier documented trends between landslide extent and volume (Fig. 13b). An alternative mobility index for landslides is calculated as $A/V^{2/3}$. The mobility coefficient for the Chaos landslide of $A/V^{2/3} \approx 10$ is at the lower end of earlier documented mobility values of high-mobility landslides (Gris-

wold and Iverson, 2008). Landslides with very high mobility coefficients are debris flows on ice or landslides in very wet environments where basal liquefaction plays a role (e.g., the OSO landslide where $A/V^{2/3} \approx 30$; Iverson et al., 2015). The lower value of $A/V^{2/3}$ for the Chaos landslide indicates limited mobility where ice and water probably played a minor role in controlling landslide runout. However, this does not mean that the changes in internal ice and water were not potential contributory factors to the 28 June collapse. Perhaps this landslide would have been more mobile if it had collapsed prior to the observed warming we document (Fig. 12), which was likely paired with a decrease in interstitial ice.
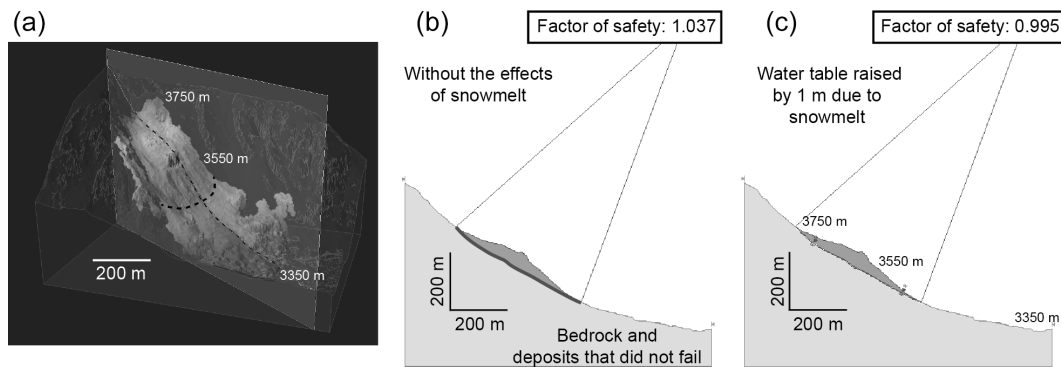
Figure 11. Output from limit equilibrium slope stability analysis. **(a)** View of the pre-collapse topography in three dimensions. The pre-collapse deposit is shown in gray. See Fig. A6 for a color version. The thick dashed line represents the lower edge of the piece of the deposit that failed on 28 June, which is also shown in **(b)** and **(c)**. The thin dashed line shows the cross section also shown in **(b)** and **(c)**. **(b)** Limit equilibrium analysis showing the global minimum slip surface and factor of safety for the simulated pre-slide deposit (purple) using the program Slide2. The failure surface (see the red line) is located at the transition between the purple body that moved during the collapse and the underlying material. **(c)** Limit equilibrium analysis showing the global minimum slip surface and factor of safety for the simulated pre-collapse deposit with the effects of a water table 1 m above the contact between the pre-collapse deposit and the underlying bedrock.
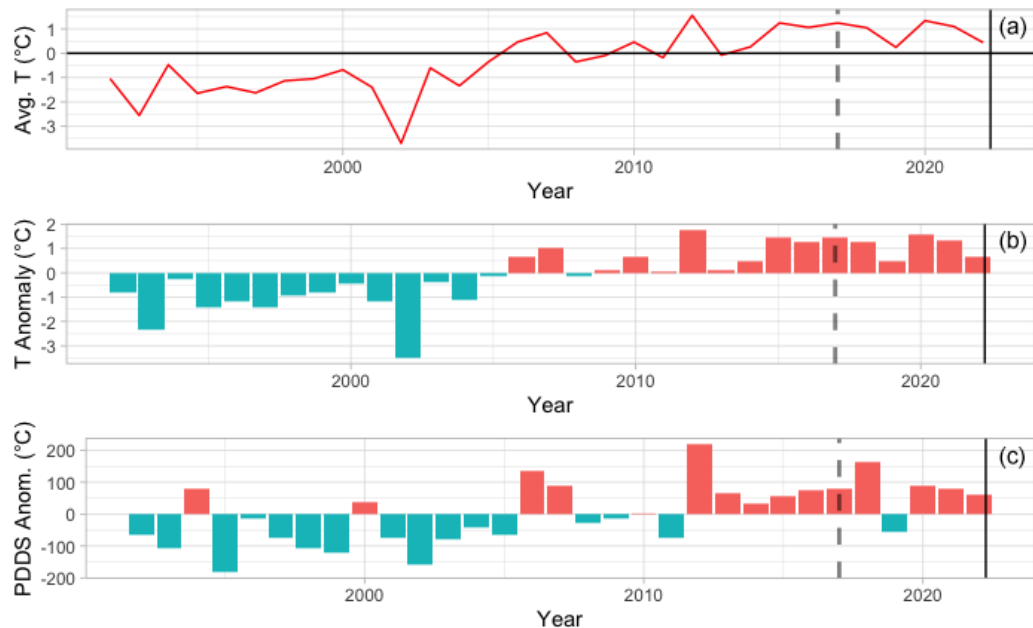
Figure 12. Temperature trends across the top of the Chaos Canyon landslide using the Bear Lake SNOTEL record and the calculated local lapse rate. Panel **(a)** shows average annual temperature from 1991 to the 2022, clearly showing a warming trend that begins in 2006. Panel **(b)** shows the annual temperature anomaly from the 31-year average; cooler colors correspond to a negative anomaly and warmer colors to a positive anomaly. Here, the warming is even more visible as a positive temperature anomaly consistent across every year after 2009. Panel **(c)** shows the PDDS anomalies calculated for the first 6 months of the calendar year for the past 31 years at the slide elevation (Braithwaite and Hughes, 2022). While the PDDS anomalies show more fluctuation than the other indicators, after ∼ 2012 the PDDS is mostly greater than in the preceding 21 years. Moreover, PDDS has been directly linked with snowmelt and is a closer proxy for potential melt that could penetrate the slide mass. The gray dashed line is the first date of image correlation data, and the dark black line is the failure date of the Chaos Canyon slide.
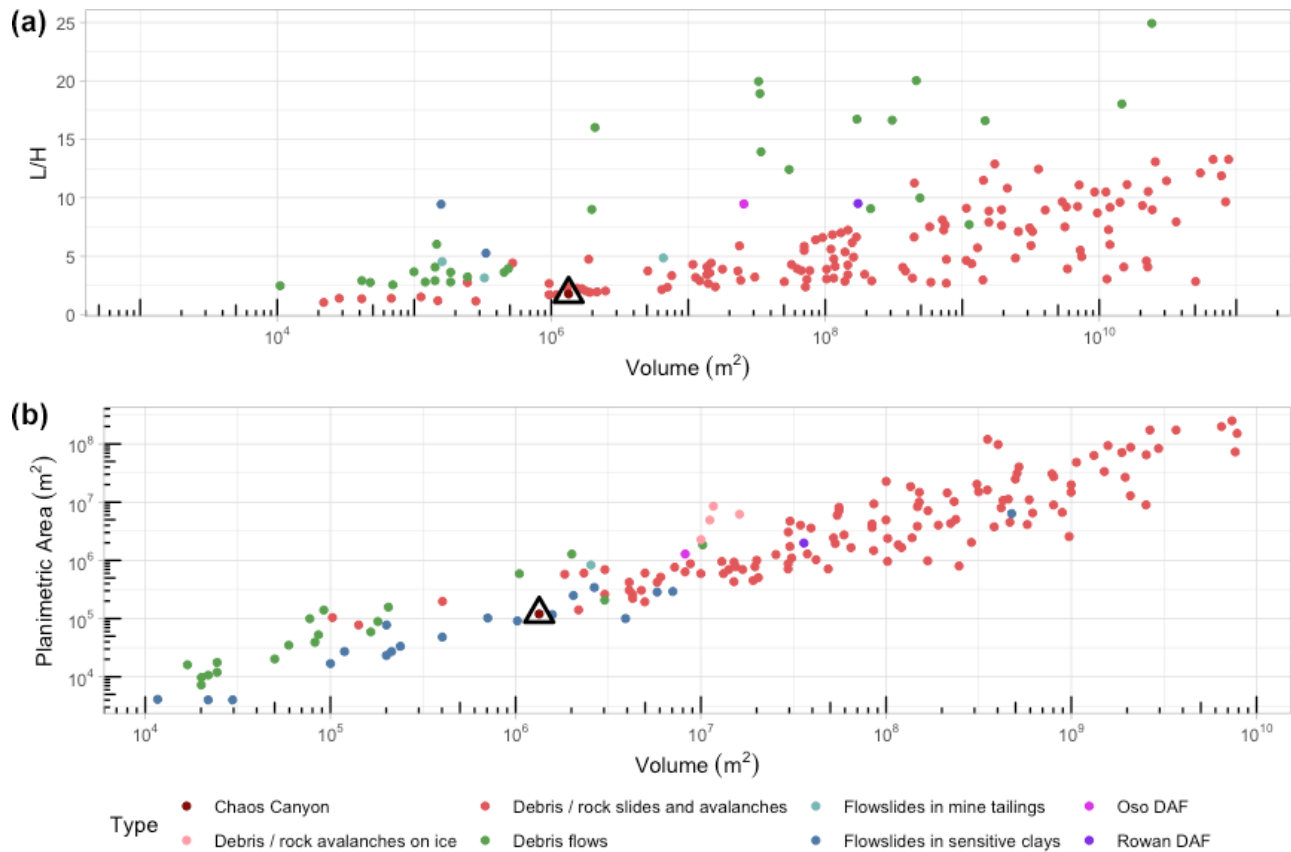
Figure 13. Landslide mobility indices. Panel **(a)** shows the commonly used maximum landslide travel path (L) over landslide height (H) versus landslide volume. The Chaos Canyon landslide (marked as a red dot with a black triangle) has a low $L/H \approx 1.8$ and falls within the field of other debris slides, rockslides, and rock avalanches (Iverson et al., 2015). Panel **(b)** shows that the Chaos Canyon landslide inundated an area consistent with a power-law relationship between landslide area and volume, as discussed in Griswold and Iverson (2008).

4.3 Are there missing alpine landscape instabilities in midlatitude North America?

The alpine regions of the coterminous United States have not, as of yet, seen a documented large increase in slope failures and rockfall linked to a warmer climate, with the Chaos Canyon landslide documented herein being a potential exception. While diagnosing this apparent lack of a landscape evolution signal tied to climate change is beyond the scope of this paper, we posit the following explanations: (1) the first is the lack of direct observations (failures are happening but not being witnessed; e.g., Huggel et al., 2012). The coterminous United States is less densely populated than Europe so there are fewer opportunities for witnesses to document failures in alpine regions. There has also not been a systematic inventory of InSAR data or permafrost across the region – put another way, there are fewer people looking for instability. For instance, the Chaos Canyon landslide was actively moving meters per year in a national park with millions of annual visitors, yet it went undetected until it failed in June 2022. (2) The second is that much of this region of North America has yet to achieve a critical threshold in permafrost thaw, snow

cover, and annual average or extreme temperatures to permit such failures to become more common. Given current emissions and committed warming, perhaps we will see more failures at an accelerating rate (e.g., Christian et al., 2018). (3) And the third is a null hypothesis. The types of slope instabilities observed in the Alps, Canadian Rockies, and Alaska are not occurring in the midlatitude mountain ranges of the coterminous United States and may not occur. We encourage others to look to these hypotheses as an opportunity for more remote sensing and field explorations of the mountainous regions of the coterminous United States.

4.4 Ramifications for alpine landscape evolution

We are witnessing a transformative period in alpine landscapes (Patton et al., 2019). The past several decades have seen changes to the ice glaciers of the world (e.g., Kääb et al., 2018), the slopes adjacent to retreating glaciers (e.g., Dai et al., 2020), rock glaciers (e.g., Bodin et al., 2017; Eriksen et al., 2018; Marcer et al., 2019), alpine rockfall (e.g., Ravanel and Deline, 2011; Deline et al., 2021), and permafrost (Patton et al., 2019). We have shown evidence

that the Chaos Canyon landslide falls within this spectrum of alpine landscape with instabilities likely tied to a warming climate (Fig. 12) and may represent an acceleration of landscape evolution that has been continuing since the Little Ice Age (1650–1850 CE Benson et al., 2007). Our change detection methods reveal that the slide translated $\sim 1\,258\,000 \pm 150\,000\,\mathrm{m}^3$ of material downslope. What we captured as part of this study is active landscape evolution, a process likely to be replicated in other alpine catchments.

The conditions documented in Chaos Canyon, an east-facing deglaciated valley which experiences higher rates of snow accumulation due to wind redistribution, are not unique in the Rocky Mountains. Where possible, mass movements should be inventoried and monitored for changing displacement rates, such as those observed in Chaos Canyon, as an indicator of a potentially impending slope failure for safety monitoring and hazard mitigation. We particularly recommend these assessments in popular recreation areas throughout the mountain west, such as the national parks. We demonstrate the utility of image correlation and the potential challenges of InSAR to detect mass movements, with repeat surveys serving to assess change over time. We caution other investigators to take an approach of combined methods – if possible, pairing image correlation with InSAR to ensure that rapidly deforming landforms are properly detected and their movement quantified with more than one method. Existing inventories indicate that permafrost is sporadic at elevations above 3200 m a.s.l. and discontinuous above 3500 m a.s.l. in Colorado and the SW US (Ives and Fahey, 1971; Obu et al., 2019). These continental-scale studies could be improved with more regional inventories of permafrost. Locations where steep slopes, identified mass movements, and permafrost intersect need further monitoring to assess future hazards – particularly in areas with large numbers of visitors. There were luckily no injuries or casualties reported with the Chaos Canyon landslide, but the increasing popularity of hiking, climbing, and other alpine activities places more people in potentially dangerous locations. It is therefore imperative to understand how and where alpine slope instabilities may occur to minimize hazards in a warming world.

5 Conclusions

The 28 June 2022 Chaos Canyon landslide provides a unique opportunity to understand rapid landscape changes in the alpine environments of the Rocky Mountain west. Moreover, the event took place in the 14th most visited national park in the country. Through our investigations, we have shown that the landslide, which translated $\sim 1\,258\,000 \pm 150\,000\,\mathrm{m}^3$, was moving up to $17\,\mathrm{m\,yr}^{-1}$ in years prior to the 28 June 2022 failure and was likely moving through a mix of both basal sliding and internal deformation. These rates of translation were fast enough to cause unwrapping errors in our InSAR observations. With an L/H mobility metric of ≈ 1.8,

the Chaos Canyon landslide could be characterized as a debris slide, rockslide, or rock avalanche, meaning the landslide had limited mobility upon collapse. A comparable landslide with greater ice content would have higher mobility and potentially prove more hazardous. The slide occurred during the peak of spring snowmelt, and the preceding 13 years were particularly warm compared to the 31-year running average. Moreover, the first 6 months of the calendar year across the past 31 years have shown higher than average positive degree days, likely impacting the timing and rate of snowmelt. We hypothesize that several years of movement, potentially leading to rate weakening of the failure surface beneath the landslide, combined with thawing of permafrost throughout the landslide body, primed the landform for failure from an increase in pore pressure. And as we documented through slope stability modeling, even a small increase in the water table leads to slope failure. We characterize the Chaos Canyon landslide as part of the broader alpine landscape evolution occurring across the high-elevation and high-latitude regions of the globe and recommend the inventorying and monitoring of such alpine landscapes to better understand where these types of hazardous slope failures may be likely to occur under a warming climate.

Appendix A

Figure A1. Photo of the slide taken from south-southwest during the SfM survey – 1 week after the collapse. Photo credit: Benjamin Lehmann.
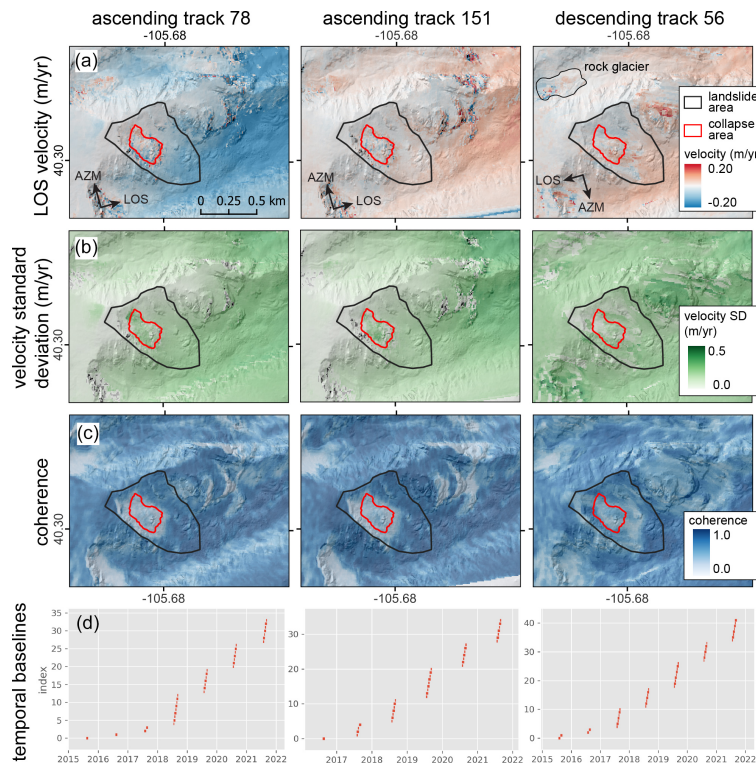

Figure A2. InSAR-derived median LOS velocity of the landslide feature prior to catastrophic failure. Sentinel-1 interferograms from ascending track 78, ascending track 151, and descending track 56 with short temporal baselines and high median coherence on the landslide slope were used to create each velocity map. **(a)** Median LOS velocity of the landslide feature and surrounding area. Positive values (red) correspond to motion away from the satellite along the satellite LOS. Note the spatial inconsistency of signals within the landslide. Apparent topography-correlated displacements are caused by atmospheric noise. **(b)** Standard deviation of median LOS velocity. **(c)** Median coherence of the landslide feature and surrounding area. Coherence is related to the similarity of scatterers in the images that form our interferograms. Note the low coherence over the landslide feature, which indicates that the surface of the feature is changing appreciably. **(d)** Temporal baselines of all available 6, 12, and 24 d Sentinel-1 interferograms from late summer. Each bar spans the temporal baseline of a single interferogram, beginning and ending at the primary and secondary acquisition dates.
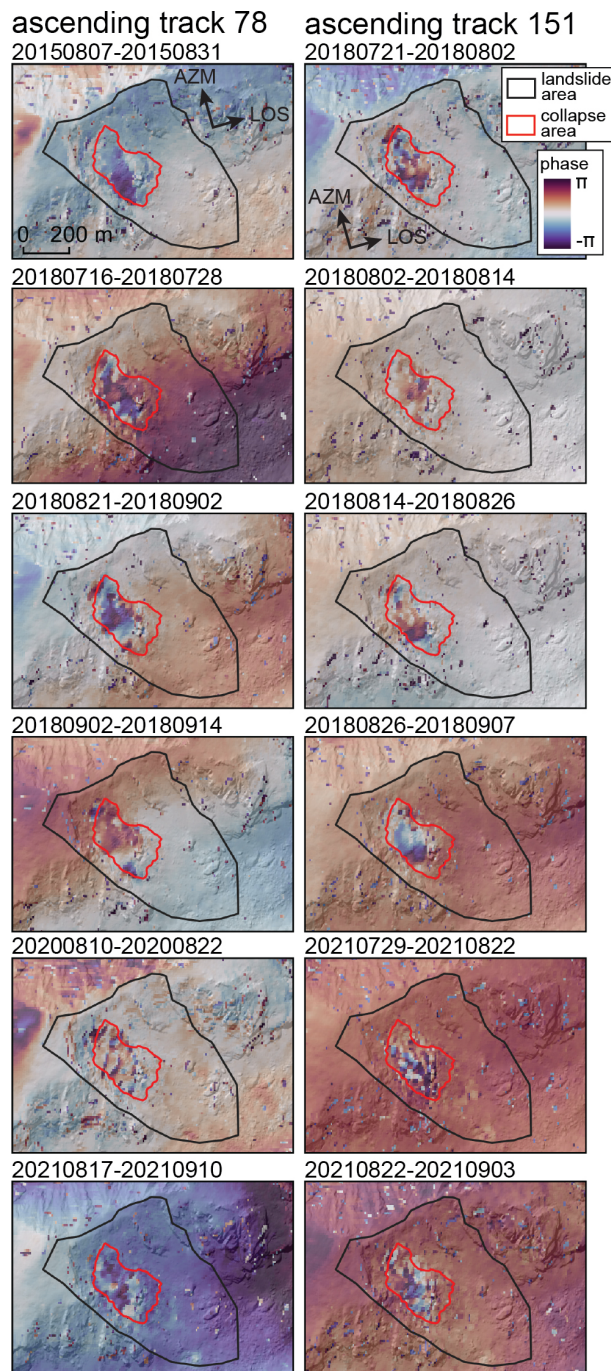
Figure A3. Wrapped short-baseline interferograms showing clear evidence of landslide displacement. Displacements more than twice the radar wavelength, as shown here, result in errors during unwrapping. The displacement signal is not as clear in other interferograms due to strong atmospheric noise and/or low coherence of the moving area. Interferograms (left) from ascending track 78. Interferograms (right) from ascending track 151.
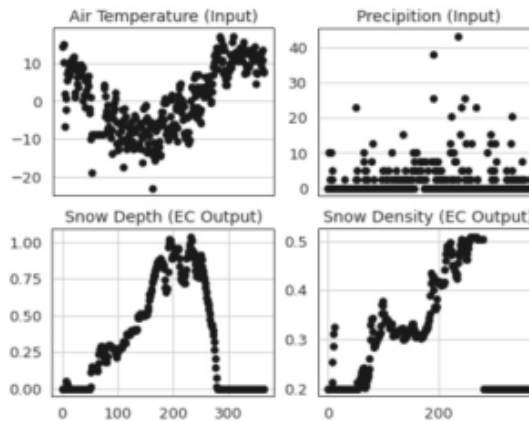
Figure A4. Simulation results of the combined snow and soil temperature model over the water year from October 2019–October 2020. Daily air temperature and precipitation inputs are derived from correcting and extrapolating the lower-elevation meteorological station at Bear Lake, RMNP. Snow depth and density are modeled by the snow model and are subsequent input for the GIPL heat conduction model.
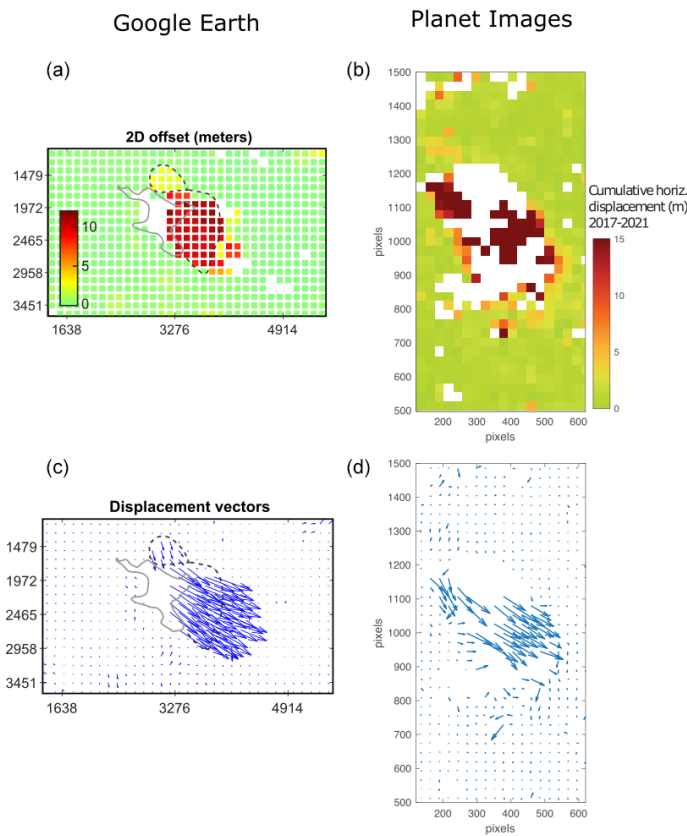
Figure A5. Direct comparison between pixel-tracking methods. Note that the Google Earth results are from 2 years of comparison; the Planet imagery includes multiple years of imagery. Panels **(a, c)** show the Google Earth method, tracking horizontal displacements over the Chaos Canyon landslide. Panels **(b, d)** show the Planet-imagery-based pixel-tracking results. While there are some differences between the results given, the different frames used, and different snowpack positions, overall the results are quite similar, with the Planet images providing more frames across multiple years than the Google Earth images.
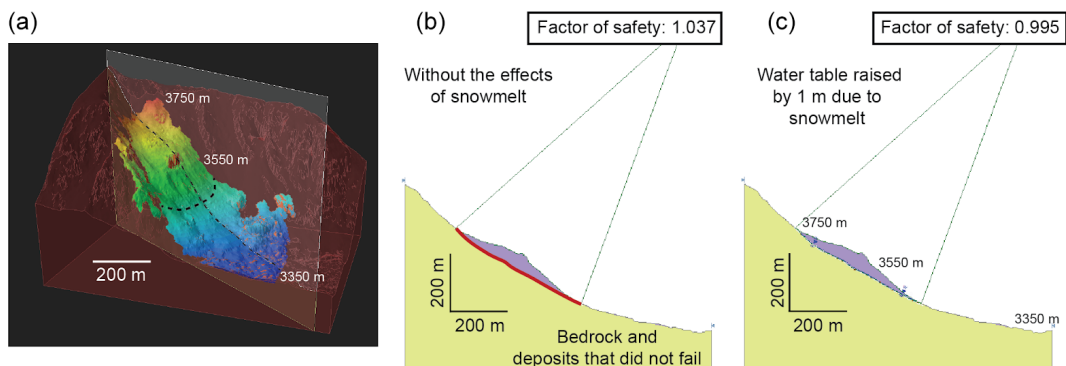
Figure A6. Output from limit equilibrium slope stability analysis. **(a)** View of the pre-collapse topography in three dimensions. The pre-collapse deposit is shown in red, yellow, and blue. The thick dashed line represents the lower edge of the deposit that failed, which is also shown in **(b)** and **(c)**. The thin dashed line shows the cross section also shown in **(b)** and **(c)**. **(b)** Limit equilibrium analysis showing the global minimum slip surface and factor of safety for the simulated pre-slide deposit (purple) using the program Slide2. The failure surface (see the red line) is located at the transition between the purple body that moved during the collapse and the underlying material. **(c)** Limit equilibrium analysis showing the global minimum slip surface and factor of safety for the simulated pre-collapse deposit with the effects of a water table 1 m above the contact between the pre-collapse deposit and the underlying bedrock.

Figure A7. Photo of the slide taken from south-southwest during the SfM survey – 1 week after the collapse. Photo credit: Benjamin Lehmann.

Table A1. Planet image pairs used in image correlation.

Image pairs	Start date (mm/dd/yy)	End date (mm/dd/yy)	Number of days
0	9/3/17	8/29/18	360
1	9/3/17	9/21/19	748
2	9/3/17	9/6/20	1099
3	9/3/17	8/28/21	1455
4	8/29/18	9/21/19	388
5	8/29/18	9/6/20	739
6	8/29/18	8/28/21	1095
7	9/21/19	9/6/20	351
8	9/21/19	8/28/21	707
9	9/6/20	8/28/21	356

Table A2. Coordinates of the stations where the photographs were acquired.

Station ID	x coord.	y coord.	z coord. (m a.s.l.)
1	105°40.044′	40°17.8760′	3462
2	105°40.1335′	40°17.8441′	3471
3	105°40.2262′	40°17.8517′	3443
4	105°40.3847′	40°17.8460′	3447
5	105°40.4287′	40°17.8296′	3452
6	105°40.5145′	40°17.7625′	3547
7	105°40.5481′	40°17.7219′	3594
8	105°40.2899′	40°17.7264′	3576
9	105°40.1936′	40°17.7611′	3547

Table A3. Ground control points X, Y, and Z, as well as total errors (cm) and error in the SfM model (px).

Label	X error (cm)	Y error (cm)	Z error (cm)	Total (cm)	Image (pix)
GCP1	0.387	−12.626	17.858	21.874	10.849 (46)
GCP2	−3.810	2.052	−19.821	20.288	13.109 (49)
GCP3	7.790	8.976	9.717	15.352	4.105 (68)
GCP5	−5.117	−9.542	−6.412	12.584	2.211 (91)
GCP4	0.686	11.160	−1.124	11.237	3.680 (48)
Total	4.517	9.589	13.028	16.795	7.296

References

Anderson, L. S., Roe, G. H., and Anderson, R. S.: The effects of interannual climate variability on the moraine record, Geology, 42, 55–58, https://doi.org/10.1130/G34791.1, 2014.

Barnes, R., Lehman, C., and Mulla, D.: Priority-flood: An optimal depression-filling and watershed-labeling algorithm for digital elevation models, Comput. Geosci., 62, 117–127, https://doi.org/10.1016/j.cageo.2013.04.024, 2014.

Benson, L., Madole, R., Kubik, P., and McDonald, R.: Surface-exposure ages of Front Range moraines that may have formed during the Younger Dryas, 8.2calka, and Little Ice Age events, Quaternary Sci. Rev., 26, 1638–1649, https://doi.org/10.1016/j.quascirev.2007.02.015, 2007.

Bickel, V. T., Manconi, A., and Amann, F.: Quantitative assessment of digital image correlation methods to detect and monitor surface displacements of large slope instabilities, Remote Sens.-Basel, 10, 865, https://doi.org/10.3390/rs10060865, 2018.

Bodin, X., Krysiecki, J.-M., Schoeneich, P., Le Roux, O., Lorier, L., Echeland, T., Peyron, M., and Walpersdorf, A.: The 2006 Collapse of the Bérard Rock Glacier (Southern French Alps): The 2006's Collapse of the Bérard Rock Glacier, Permafrost Periglac., 28, 209–223, https://doi.org/10.1002/ppp.1887, 2017.

Bogaard, T. A. and Greco, R.: Landslide hydrology: from hydrology to pore pressure, WIREs Water, 3, 439–459, https://doi.org/10.1002/wat2.1126, 2016.

Braddock, W. and Cole, J.: Geologic Map of Rocky Mountain National Park and Vicinity, Colorado, USGS Numbered Series 1973, U. S. Geological Survey, 1990.

Braithwaite, R. J. and Hughes, P. D.: Positive degree-day sums in the Alps: a direct link between glacier melt and international climate policy, J. Glaciol., 68, 901–911, https://doi.org/10.1017/jog.2021.140, 2022.

Brown, R. D., Brasnett, B., and Robinson, D.: Gridded North American monthly snow depth and snow water equivalent for GCM evaluation, Atmosphere-Ocean, 41, 1–14, https://doi.org/10.3137/ao.410101, 2003.

Bürgmann, R., Rosen, P. A., and Fielding, E. J.: Synthetic Aperture Radar Interferometry to Measure Earth's Surface Topography and Its Deformation, Annu. Rev. Earth Pl. Sc., 28, 169–209, https://doi.org/10.1146/annurev.earth.28.1.169, 2000.

Carson, M. A.: Angles of repose, angles of shearing resistance and angles of talus slopes, Earth Surf. Processes, 2, 363–380, https://doi.org/10.1002/esp.3290020408, 1977.

Christian, J. E., Koutnik, M., and Roe, G.: Committed retreat: controls on glacier disequilibrium in a warming climate, J. Glaciol., 64, 675–688, https://doi.org/10.1017/jog.2018.57, 2018.

Cossart, E., Braucher, R., Fort, M., Bourlès, D., and Carcaillet, J.: Slope instability in relation to glacial debuttressing in alpine areas (Upper Durance catchment, southeastern France): Evidence from field data and 10Be cosmic ray exposure ages, Geomorphology, 95, 3–26, https://doi.org/10.1016/j.geomorph.2006.12.022, 2008.

Cruden, D. and Varnes, D.: Landslide Types and Processes, U.S. National Academy of Sciences, Special Report, National Research Council, Transportation Research Board, 247, 36–57, https://www.researchgate.net/profile/David-Cruden/publication/295704933_TEXT_of_1993_DRAFT/links/56ccd62f08aeb52500c09e29/TEXT-of-1993-DRAFT.pdf (last access: 12 September 2023) 1996.

Dai, C., Higman, B., Lynett, P. J., Jacquemart, M., Howat, I. M., Liljedahl, A. K., Dufresne, A., Freymueller, J. T., Geertsema, M., Ward Jones, M., and Haeussler, P. J.: Detection and Assessment of a Large and Potentially Tsunamigenic Periglacial Landslide in Barry Arm, Alaska, Geophys. Res. Lett., 47, e2020GL089800, https://doi.org/10.1029/2020GL089800, 2020.

Deline, P., Gruber, S., Amann, F., Bodin, X., Delaloye, R., Failletaz, J., Fischer, L., Geertsema, M., Giardino, M., Hasler, A., Kirkbride, M., Krautblatter, M., Magnin, F., McColl, S., Ravanel, L., Schoeneich, P., and Weber, S.: Ice loss from glaciers and permafrost and related slope instability in high-mountain regions, in: Snow and Ice-Related Hazards, Risks, and Disasters, Elsevier, 501–540, https://doi.org/10.1016/B978-0-12-817129-5.00015-9, 2021.

Dematteis, N., Giordan, D., Troilo, F., Wrzesniak, A., and Godone, D.: Ten-Year Monitoring of the Grandes Jorasses Glaciers Kinematics. Limits, Potentialities, and Possible Applications of Different Monitoring Systems, Remote Sens.-Basel, 13, 3005, https://doi.org/10.3390/rs13153005, 2021.

Duncan, J. M.: State of the Art: Limit Equilibrium and Finite-Element Analysis of Slopes, J. Geotech. Eng.-ASCE, 122, 577–596, https://doi.org/10.1061/(ASCE)0733-9410(1996)122:7(577), 1996.

Duncan, J. M.: Factors of Safety and Reliability in Geotechnical Engineering, J. Geotech. Geoenviron., 126, 307–316, https://doi.org/10.1061/(ASCE)1090-0241(2000)126:4(307), 2000.

Eberhardt, E., Preisig, G., and Gischig, V.: Progressive failure in deep-seated rockslides due to seasonal fluctuations in pore pressures and rock mass fatigue, in: Landslides and Engineered Slopes. Experience, Theory and Practice, CRC Press, 16 pp., ISBN 9781315375007, 2016.

Eriksen, H. Ø., Rouyet, L., Lauknes, T. R., Berthling, I., Isaksen, K., Hindberg, H., Larsen, Y., and Corner, G. D.: Recent Acceleration of a Rock Glacier Complex, Ádjet, Norway, Documented by 62 Years of Remote Sensing Observations, Geophys. Res. Lett., 45, 8314–8323, https://doi.org/10.1029/2018GL077605, 2018.

Fukozono, T.: Recent studies on time prediction of slope failure, Landslide News, 4, 9–12, https://cir.nii.ac.jp/crid/1570572699789681280 (last access: 11 September 2023), 1990.

Geertsema, M., Schwab, J. W., Blais-Stevens, A., and Sakals, M. E.: Landslides impacting linear infrastructure in west central British Columbia, Nat. Hazards, 48, 59–72, https://doi.org/10.1007/s11069-008-9248-0, 2009.

Geertsema, M., Menounos, B., Bullard, G., Carrivick, J. L., Clague, J. J., Dai, C., Donati, D., Ekstrom, G., Jackson, J. M., Lynett, P., Pichierri, M., Pon, A., Shugar, D. H., Stead, D., Del Bel Belluz, J., Friele, P., Giesbrecht, I., Heathfield, D., Millard, T., Nasonova, S., Schaeffer, A. J., Ward, B. C., Blaney, D., Blaney, E., Brillon, C., Bunn, C., Floyd, W., Higman, B., Hughes, K. E., McInnes, W., Mukherjee, K., and Sharp, M. A.: The 28 November 2020 Landslide, Tsunami, and Outburst Flood – A Hazard Cascade Associated With Rapid Deglaciation at Elliot Creek, British Columbia, Canada, Geophys. Res. Lett., 49, e2021GL096716, https://doi.org/10.1029/2021GL096716, 2022.

Giordan, D., Dematteis, N., Allasia, P., and Motta, E.: Classification and kinematics of the Planpincieux Glacier break-offs using photographic time-lapse analysis, J. Glaciol., 66, 188–202, https://doi.org/10.1017/jog.2019.99, 2020.

Goodrich, L. E.: The influence of snow cover on the ground thermal regime, Can. Geotech. J., 19, 421–432, https://doi.org/10.1139/t82-047, 1982.

Griswold, R. and Iverson, R.: Mobility Statistics and Automated Hazard Maapping for Debris Flows and Rock Avalanches, Scientific Investigations Report 2007-5276, U. S. Geological Survey, https://pubs.usgs.gov/sir/2007/5276/sir2007-5276.pdf (last access: 11 September 2023), 2008.

Handwerger, A. L., Roering, J. J., Schmidt, D. A., and Rempel, A. W.: Kinematics of earthflows in the Northern California Coast Ranges using satellite interferometry, Geomorphology, 246, 321–333, https://doi.org/10.1016/j.geomorph.2015.06.003, 2015.

Hengl, T., de Jesus, J. M., MacMillan, R. A., Batjes, N. H., Heuvelink, G. B. M., Ribeiro, E., Samuel-Rosa, A., Kempen, B., Leenaars, J. G. B., Walsh, M. G., and Gonzalez, M. R.: SoilGrids1km – Global Soil Information Based on Automated Mapping, PLoS ONE, 9, e105992, https://doi.org/10.1371/journal.pone.0105992, 2014.

Huggel, C., Salzmann, N., Allen, S., Caplan-Auerbach, J., Fischer, L., Haeberli, W., Larsen, C., Schneider, D., and Wessels, R.: Recent and future warm extreme events and high-mountain slope stability, Philos. T. Roy. Soc. A, 368, 2435–2459, https://doi.org/10.1098/rsta.2010.0078, 2010.

Huggel, C., Clague, J. J., and Korup, O.: Is climate change responsible for changing landslide activity in high mountains?: Climate change and landslides in high mountains, Earth Surf. Processes, 37, 77–91, https://doi.org/10.1002/esp.2223, 2012.

Hugonnet, R., McNabb, R., Berthier, E., Menounos, B., Nuth, C., Girod, L., Farinotti, D., Huss, M., Dussaillant, I., Brun, F., and Kääb, A.: Accelerated global glacier mass loss in the early twenty-first century, Nature, 592, 726–731, https://doi.org/10.1038/s41586-021-03436-z, 2021.

Ito, Y. and Ikari, M. J.: Velocity- and slip-dependent weakening in simulated fault gouge: Implications for multimode fault slip: Velocity- and slip-dependent friction, Geophys. Res. Lett., 42, 9247–9254, https://doi.org/10.1002/2015GL065829, 2015.

Itoh, K.: Analysis of the phase unwrapping algorithm, Appl. Optics, 21, 2470–2470, https://doi.org/10.1364/AO.21.002470, 1982.

Iverson, R. M., George, D. L., Allstadt, K., Reid, M. E., Collins, B. D., Vallance, J. W., Schilling, S. P., Godt, J. W., Cannon, C. M., Magirl, C. S., Baum, R. L., Coe, J. A., Schulz, W. H., and Bower, J. B.: Landslide mobility and hazards: implications of the 2014 Oso disaster, Earth Planet. Sc. Lett., 412, 197–208, https://doi.org/10.1016/j.epsl.2014.12.020, 2015.

Ives, J. D. and Fahey, B. D.: Permafrost Occurrence in the Front Range, Colorado Rocky Mountains, U.S.A., J. Glaciol., 10, 105–111, https://doi.org/10.3189/S0022143000013034, 1971.

Jafarov, E. E., Marchenko, S. S., and Romanovsky, V. E.: Numerical modeling of permafrost dynamics in Alaska using a high spatial resolution dataset, The Cryosphere, 6, 613–624, https://doi.org/10.5194/tc-6-613-2012, 2012.

Johnson, G., Chang, H., and Fountain, A.: Active rock glaciers of the contiguous United States: geographic information system inventory and spatial distribution patterns, Earth Syst. Sci. Data, 13, 3979–3994, https://doi.org/10.5194/essd-13-3979-2021, 2021.

Kääb, A., Leinss, S., Gilbert, A., Bühler, Y., Gascoin, S., Evans, S. G., Bartelt, P., Berthier, E., Brun, F., Chao, W.-A., Farinotti, D., Gimbert, F., Guo, W., Huggel, C., Kargel, J. S., Leonard, G. J., Tian, L., Treichler, D., and Yao, T.: Massive collapse of two glaciers in western Tibet in 2016 after surge-like instability, Nat. Geosci., 11, 114–120, https://doi.org/10.1038/s41561-017-0039-7, 2018.

Kenner, R., Phillips, M., Beutel, J., Hiller, M., Limpach, P., Pointner, E., and Volken, M.: Factors Controlling Velocity Variations at Short-Term, Seasonal and Multiyear Time Scales, Ritigraben Rock Glacier, Western Swiss Alps, Permafrost Periglac., 28, 675–684, https://doi.org/10.1002/ppp.1953, 2017.

Kersten, M. S.: Thermal properties of soils, vol. 52, University of Minnesota – Institute of Technology, https://conservancy.umn.edu/bitstream/handle/11299/124271/eng_ex_bulletin_28.pdf?sequence=1 (last access: 10 September 2023), 1949.

Kos, A., Amann, F., Strozzi, T., Delaloye, R., Ruette, J., and Springman, S.: Contemporary glacier retreat triggers a rapid landslide response, Great Aletsch Glacier, Switzerland, Geophys. Res. Lett., 43, 2016GL071708, https://doi.org/10.1002/2016GL071708, 2016.

Labuz, J. F. and Zang, A.: Mohr–Coulomb Failure Criterion, Rock Mech. Rock Eng., 45, 975–979, https://doi.org/10.1007/s00603-012-0281-7, 2012.

Lacroix, P., Belart, J. M. C., Berthier, E., Sæmundsson, Þ., and Jónsdóttir, K.: Mechanisms of Landslide Destabilization Induced by Glacier-Retreat on Tungnakvíslarjökull Area, Iceland, Geophys. Res. Lett., 49, e2022GL098302, https://doi.org/10.1029/2022GL098302, 2022.

Lipovsky, P. S., Evans, S. G., Clague, J. J., Hopkinson, C., Couture, R., Bobrowsky, P., Ekström, G., Demuth, M. N., Delaney, K. B., Roberts, N. J., Clarke, G., and Schaeffer, A.: The July 2007 rock and ice avalanches at Mount Steele, St. Elias Mountains, Yukon, Canada, Landslides, 5, 445–455, https://doi.org/10.1007/s10346-008-0133-4, 2008.

Marcer, M., Serrano, C., Brenning, A., Bodin, X., Goetz, J., and Schoeneich, P.: Evaluating the destabilization susceptibility of active rock glaciers in the French Alps, The Cryosphere, 13, 141–155, https://doi.org/10.5194/tc-13-141-2019, 2019.

Marzeion, B., Cogley, J. G., Richter, K., and Parkes, D.: Attribution of global glacier mass loss to anthropogenic and natural causes, Science, 345, 919–921, https://doi.org/10.1126/science.1254702, 2014.

Milliner, C. and Donnellan, A.: Using Daily Observations from Planet Labs Satellite Imagery to Separate the Surface Deformation between the 4 July Mw 6.4 Foreshock and 5 July Mw 7.1 Mainshock during the 2019 Ridgecrest Earthquake Sequence, Seismol. Res. Lett., 91, 1986–1997, https://doi.org/10.1785/0220190271, 2020.

Morriss, M. C., Lehmann, B., Campforts, B., Brencher, G., Rick, B., Anderson, L., Handwerger, A., Overeem, I., and Moore, J.: Alpine hillslope failure in the western US: Insights from Chaos Canyon landslide, Rocky Mountain National Park USA, Zenodo [code and data set], https://doi.org/10.5281/zenodo.7854068, 2023.

Mutter, E. Z. and Phillips, M.: Thermal Evidence of Recent Talik Formation in Ritigraben Rock Glacier: Swiss Alps, in: Proceedings of the 10th International Conference on Permafrost, The Northern Publisher, Salekhard, Russia, 25–29 June 2012, 479–483, https://www.dora.lib4ri.ch/wsl/islandora/object/wsl%3A20703 (last access: 14 September 2023), 2012.

NPS: NPS Visitation Numbers, https://www.nps.gov/aboutus/visitation-numbers.htm (last access: 10 October 2023), 2022.

NRCS: SNOwpack TELemetry Network (SNOTEL), https://data.nal.usda.gov/dataset/snowpack-telemetry-network-snotel (last access: 7 February 2023), 2023.

Obu, J., Westermann, S., Bartsch, A., Berdnikov, N., Christiansen, H. H., Dashtseren, A., Delaloye, R., Elberling, B., Etzelmüller, B., Kholodov, A., Khomutov, A., Kääb, A., Leibman, M. O., Lewkowicz, A. G., Panda, S. K., Romanovsky, V., Way, R. G., Westergaard-Nielsen, A., Wu, T., Yamkhin, J., and Zou, D.: Northern Hemisphere permafrost map based on TTOP modelling for 2000–2016 at $1\,\mathrm{km}^2$ scale, Earth-Sci. Rev., 193, 299–316, https://doi.org/10.1016/j.earscirev.2019.04.023, 2019.

O'Connor, J. E. and Costa, J. E.: Geologic and hydrologic hazards in glacierized basins in North America resulting from 19th and 20th century global warming, Nat. Hazards, 8, 121–140, https://doi.org/10.1007/BF00605437, 1993.

Overeem, I., Jafarov, E., Wang, K., Schaefer, K., Stewart, S., Clow, G., Piper, M., and Elshorbany, Y.: A Modeling Toolbox for Permafrost Landscapes, Eos, 99, https://doi.org/10.1029/2018EO105155, 2018.

Patton, A. I., Rathburn, S. L., and Capps, D. M.: Landslide response to climate change in permafrost regions, Geomorphology, 340, 116–128, https://doi.org/10.1016/j.geomorph.2019.04.029, 2019.

Planet-Team: Planet Application Program Interface: In space for Life on Earth, https://api.planet.com (last access: y), 2017.

Pudasaini, S. P. and Krautblatter, M.: A two-phase mechanical model for rock-ice avalanches, J. Geophys. Res.-Earth, 119, 2272–2290, https://doi.org/10.1002/2014JF003183, 2014.

Ravanel, L. and Deline, P.: Climate influence on rockfalls in high-Alpine steep rockwalls: The north side of the Aiguilles de Chamonix (Mont Blanc massif) since the end of the "Little Ice Age", Holocene, 21, 357–365, https://doi.org/10.1177/0959683610374887, 2011.

Rocscience: Slide 2 2D Limit Equilibrium Slope Stability for Soil and Rock Slopes, https://www.rocscience.com/software/slide2 (last access: 2 April 2023) 2021.

Rosen, P. A., Gurrola, E., Sacco, G. F., and Zebker, H.: The InSAR scientific computing environment, in: EUSAR 2012, 9th European Conference on Synthetic Aperture Radar, Nuremberg, Germany, 23–26 April 2012, 730–733, 2012.

Schaefer, K. and Jafarov, E.: A parameterization of respiration in frozen soils based on substrate availability, Biogeosciences, 13, 1991–2001, https://doi.org/10.5194/bg-13-1991-2016, 2016.

Scuderi, M., Collettini, C., and Marone, C.: Frictional stability and earthquake triggering during fluid pressure stimulation of an experimental fault, Earth Planet. Sc. Lett., 477, 84–96, https://doi.org/10.1016/j.epsl.2017.08.009, 2017.

Shan, W., Guo, Y., Wang, F., Marui, H., and Strom, A. (Eds.): Landslides in Cold Regions in the Context of Climate Change, Environmental Science and Engineering, Springer International Publishing, Cham, https://doi.org/10.1007/978-3-319-00867-7, 2014.

Slater, A. G. and Lawrence, D. M.: Diagnosing Present and Future Permafrost from Climate Models, J. Climate, 26, 5608–5623, https://doi.org/10.1175/JCLI-D-12-00341.1, 2013.

Stoffel, M. and Huggel, C.: Effects of climate change on mass movements in mountain environments, Progress in Physical Geography: Earth and Environment, 36, 421–439, https://doi.org/10.1177/0309133312441010, 2012.

Sturm, M., Holmgren, J., and Liston, G.: A seasonal snow cover classification system for local to global applications, J. Climate, 8, 1261–1283, 1995.

USGS: National Hydrography Dataset (ver. USGS National Hydrography Dataset Best Resolution (NHD), http://prd-tnm. s3-website-us-west-2.amazonaws.com/?prefix=StagedProducts/ Hydrography/NHD/HU4/HighResolution/GDB/ (last access: 2 October 2022), 2019.

Viesca, R. C. and Rice, J. R.: Nucleation of slip-weakening rupture instability in landslides by localized increase of pore pressure, J. Geophys. Res.-Sol. Ea., 117, B03104, https://doi.org/10.1029/2011JB008866, 2012.

Voight, B.: A Relation to Describe Rate-Dependent Material Failure, Science, 243, 200–203, https://doi.org/10.1126/science.243.4888.200, 1989.

Whalley, W. B. and Martin, H. E.: Rock glaciers: II models and mechanisms, Progress in Physical Geography: Earth and Environment, 16, 127–186, https://doi.org/10.1177/030913339201600201, 1992.

Yunjun, Z., Fattahi, H., and Amelung, F.: Small baseline InSAR time series analysis: Unwrapping error correction and noise reduction, Comput. Geosci., 133, 104331, https://doi.org/10.1016/j.cageo.2019.104331, 2019.

Zhang, T.: Influence of the seasonal snow cover on the ground thermal regime: An overview: Snow cover and ground thermal regime, Rev. Geophys., 43, RG4002, https://doi.org/10.1029/2004RG000157, 2005.